ARTICLE OPEN

Suppression of mitochondrial energy production by a photosynthetic bacterial cupredoxin peptide inhibits tumor growth

Samer A. Naffouje[1,5], Duy Binh Tran[1], David J. Rademacher[2], Valentina Botti[3], Konstantin Christov[1], Albert Green[1], Weiguo Li[4], Ngoc Hai Trieu Phong[1], Salvatore Cannistraro[3], Anna Rita Bizzarri[3], Tapas K. Das Gupta[1] and Tohru Yamada[1,4]✉

Accumulating evidence shows that bacteria influence cancer homeostasis, yet the effects of tumor-associated microbes and their products remain largely unexplored. We previously reported that *P. aeruginosa*–cancer crosstalk suppresses tumors via the bacterial cupredoxin azurin, and we developed an azurin-derived peptide that was tested in clinical trials. Building on our previous studies, we studied tumor-resident bacteria for novel therapeutics and targets. Photosynthetic bacteria from the phylum Chloroflexota, including a member of the class Chloroflexia, identified in tumors, carry the cupredoxin auracyanin gene. Based on the structural and chemical characteristics of auracyanin, we designed a novel cell-penetrating peptide, aurB. Plant chloroplasts are thought to have evolved from a bacterial endosymbiont, and both chloroplasts and mitochondria possess shared proteins essential for ATP-dependent energy production, indicating that these bacterial-derived proteins may influence mitochondrial function. Consistent with this model, we demonstrated that aurB, a peptide from cupredoxin auracyanin B, localized at mitochondria, blocked energy production by targeting ATP synthase in prostate cancer cells, thereby significantly inhibiting tumor growth. More strikingly, combination treatment with aurB and radiation therapy significantly inhibited tumor growth in a tibial bone metastasis model. Moreover, the number of metastatic lesions in the lungs was also significantly lower upon aurB treatment. Multiplex RNA-expression profiling revealed that the inhibition of ATP production by aurB increased the efficacy of radiation therapy by modulating multiple pathways involving HIF-1α. Our findings indicate that electron transfer proteins could represent an important source of promising novel peptide-based agents that target the aberrantly activated mitochondrial energy system in cancer.

Signal Transduction and Targeted Therapy (2026)11:124 ; https://doi.org/10.1038/s41392-026-02703-7

INTRODUCTION

There have been many advances in the development of targeted cancer treatments. Mitochondria have been recognized as among the most important targets for the development of new therapeutic agents. Mitochondrial functions in eukaryotes include ATP generation and the regulation of cell proliferation and death. Abnormal mitochondrial function has long been associated with aberrant cancer cell proliferation.[1] Furthermore, mitochondrial ATP synthesis is often altered in cancer cells and plays a crucial role in tumor growth and patient overall survival.[2–4] Therefore, targeting mitochondria in cancer cells is a promising approach for the development of new therapeutic agents. However, traditional chemotherapeutic agents that target mitochondria generally do so indirectly by targeting upstream signaling pathways that are frequently impaired or inactivated in cancer (*e.g.*, p53), including advanced prostate and ovarian cancer, two cancer types that are typically lethal and exhibit a limited response to immune checkpoint inhibitors.[5,6] Thus, new therapeutic agents that target mitochondria in cancer cells would be ideal.

Eukaryotes have coevolved with diverse microbial communities, including bacteria. According to the endosymbiotic theory, mitochondria and chloroplasts originated from the engulfment of symbiotic bacteria by ancestral eukaryotes; mitochondria arose early in eukaryotic evolution (over 1 billion years ago), and chloroplasts arose somewhat later via endosymbiosis of a cyanobacterium in the ancestor of photosynthetic eukaryotes.[7,8] As such, electron-transfer proteins that generate energy (*e.g.*, ATP) in bacteria, chloroplasts, and mitochondria share high levels of structural and functional homology.[9–11] For instance, one of protein families expressed in chloroplasts and mitochondria is the cupredoxin family, which consists of blue copper proteins comprising an eight-stranded Greek key β-barrel with a distinctive class α/β parallel connection.[12,13] Cupredoxin superfamily proteins are found in several kingdoms and are therefore universally important to organisms.[14] For example, mitochondrial genome sequencing studies have revealed proteins with homology to bacterial cupredoxins in the mitochondria of eukaryotes, such as sunflower plants (*Helianthus*).[15] Cupredoxin plastocyanin plays a role in photosynthetic electron transport within chloroplasts in plants.[16]

[1]Department of Surgery, Division of Surgical Oncology, University of Illinois College of Medicine, Chicago, IL, USA; [2]Department of Microbiology and Immunology and Core Microscopy Facility, Loyola University Chicago, Chicago, IL, USA; [3]Biophysics and Nanoscience Centre, Department of Ecology and Biology, Università della Tuscia, Viterbo, Italy, [4]Richard & Loan Hill Department of Bioengineering, University of Illinois, College of Engineering, Chicago, IL, USA and [5]Present address: General Surgery, Cleveland Clinic, Cleveland, OH, USA
Correspondence: Tohru Yamada (tohru@uic.edu)
These authors contributed equally: Samer A. Naffouje, Duy Binh Tran

Received: 18 April 2025 Revised: 29 January 2026 Accepted: 17 March 2026
Published online: 07 April 2026

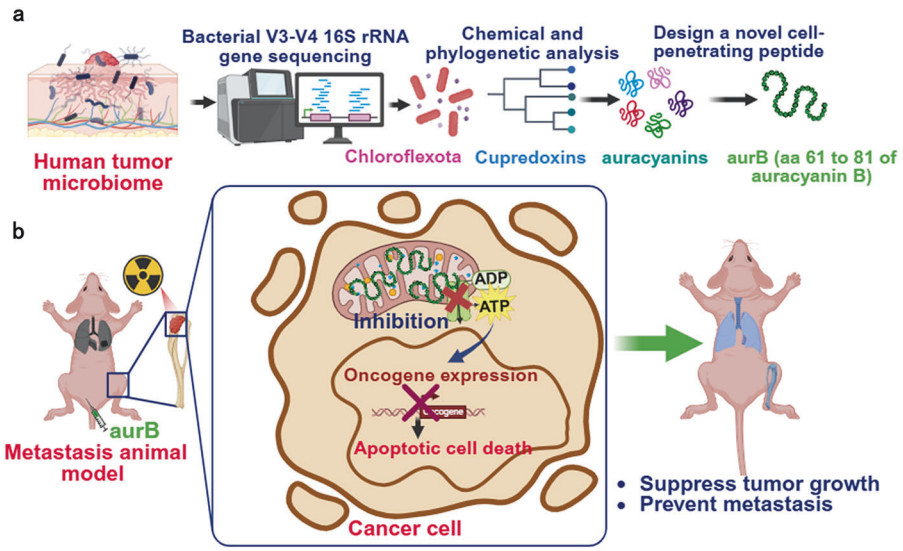

Fig. 1 Schematic representation of the innovative peptide design and treatment of a preclinical tumor model. The peptide was designed through characterizations of the bacterial 16S rRNA gene in human tumors, combined with chemical and phylogenetic analysis (**a**). The aurB peptide enhances radiation sensitivity in tumors through the inhibition of mitochondrial energy production and downregulation of oncogenes, thereby suppressing significant tumor growth and metastasis (**b**). Created in BioRender, https://BioRender.com

Moreover, in several types of bacteria, cupredoxins are involved in electron transfer in a variety of biological processes, including energy production through nitrogen fixation and photosynthesis.[17,18]

We previously demonstrated that a peptide derived from the electron transfer cupredoxin azurin in nonphotosynthetic *Pseudomonas aeruginosa* (referred to as p28; NSC745104) induced p53-dependent tumor growth inhibition in animal models of a broad range of cancer types[19–26] and showed preliminary efficacy in two phase I clinical trials without apparent toxicity in patients with advanced solid tumors and pediatric patients with recurrent and refractory central nervous system (CNS) tumors (NCI, Pediatric Brain Tumor Consortium).[27–29] Unlike cupredoxin proteins from nonphotosynthetic bacteria, we focus on a cupredoxin protein from photosynthetic bacteria for novel therapeutics and targets based on our concept. Given that the electron transfer system in photosynthetic bacteria is crucial for converting energy and is substantially different from that in nonphotosynthetic bacteria,[30] we hypothesized that cupredoxin in photosynthetic bacteria might be a unique source for novel therapeutics. Although it is not very common, there are a few reports describing that photosynthetic bacteria are found in humans,[31,32] and we also detected the photosynthetic bacteria Chloroflexia in human tumor samples in this study. They have cupredoxin proteins called auracyanin that are involved in electron transfer chains during photosynthesis.[33] Furthermore, auracyanin is reported to be a descendant of an ancestral sequence common to both the azurin proteins expressed by prokaryotic nonphotosynthetic bacteria and the cupredoxin plastocyanin proteins expressed by both prokaryotic bacteria and eukaryotic algae and plants.[34] Considering this evidence, we focused on auracyanin, designed a novel cell-penetrating peptide based on chemical and phylogenetic characteristics (Fig. 1a), and studied its biological functions in mitochondria and the effects on cancer proliferation in comparative in vitro and in vivo models, including a tibial bone metastasis model (Fig. 1b). This is the first study to demonstrate the molecular mechanisms through which a novel anticancer peptide originating from a photosynthetic bacterial protein specifically interacts with mitochondria.

RESULTS

Identification and design of an auracyanin-derived peptide

Accumulating evidence suggests that microorganisms such as bacteria play important roles in cancer homeostasis.[35,36] We previously showed that crosstalk between cancer (e.g., breast cancer and melanoma) and the opportunistic pathogen *Pseudomonas aeruginosa* mediates tumor suppression.[37] It is mediated by the cupredoxin azurin from *P. aeruginosa*. While bacteria within human tumors, known as the tumor microbiome, have been recently characterized,[38] the impact of these bacteria and their products has not been widely explored. Thus, we first characterized the bacterial populations in tumors from primary and metastatic breast cancer by the bacterial 16S rRNA gene[39] (Supplementary Fig. S1a, b). Consistent with previous reports,[40] our results showed that Proteobacteria were abundant in tumor tissues (Supplementary Fig. S1c). In contrast, no bacterial populations were detected in the mouse brain tissues as a negative control. Proteobacteria include a wide variety of pathogenic bacteria (e.g., azurin-expressing Pseudomonas). As we have been studying cupredoxins such as type-I blue copper protein azurin, we generated a phylogenetic tree for bacterial cupredoxins to identify homologous proteins, which revealed auracyanins as the closest to azurin (Supplementary Fig. S1d). In the tumor microbiome we analyzed (Supplementary Fig. S1c), bacteria of the phylum Chloroflexota—including members of the class photosynthetic Chloroflexia (ranked 13th in abundance in this analysis)—harbor cupredoxin auracyanin genes. To investigate the diversity of such family proteins within the phylum Chloroflexota, we searched UniProt for cupredoxin domain-containing proteins (Supplementary Fig. S1e). While multiple entries annotated as “cupredoxin-like” or “blue copper-binding” were found (e.g., UniProt IDs A0A933VBB6, A0A7C1KCA4, A0A9E4VIU8, A0A535HE61, A0A8K0ZFD4), only auracyanins (e.g., Q8RMH6, P27197) were experimentally validated. The other entries represent unreviewed predictions based solely on sequence similarity or domain architecture and lack structural or functional confirmation. These findings, which identify auracyanins as the confirmed single-domain blue copper proteins in Chloroflexota, prompted us to investigate further. Based on Supplementary Fig. S1e, auracyanins (auracyanin A and B) are the closest proteins to azurin. Given that interest in therapeutic peptides has surged due to recent advances in their delivery, synthesis, design, and clinical viability, we designed and identified the cell-penetrating peptide p28 from azurin,[24,41,42] which adopts a structure containing α-helical and β-sheet motifs and random coils in solution.[25] Similarly, our early phase studies indicated that

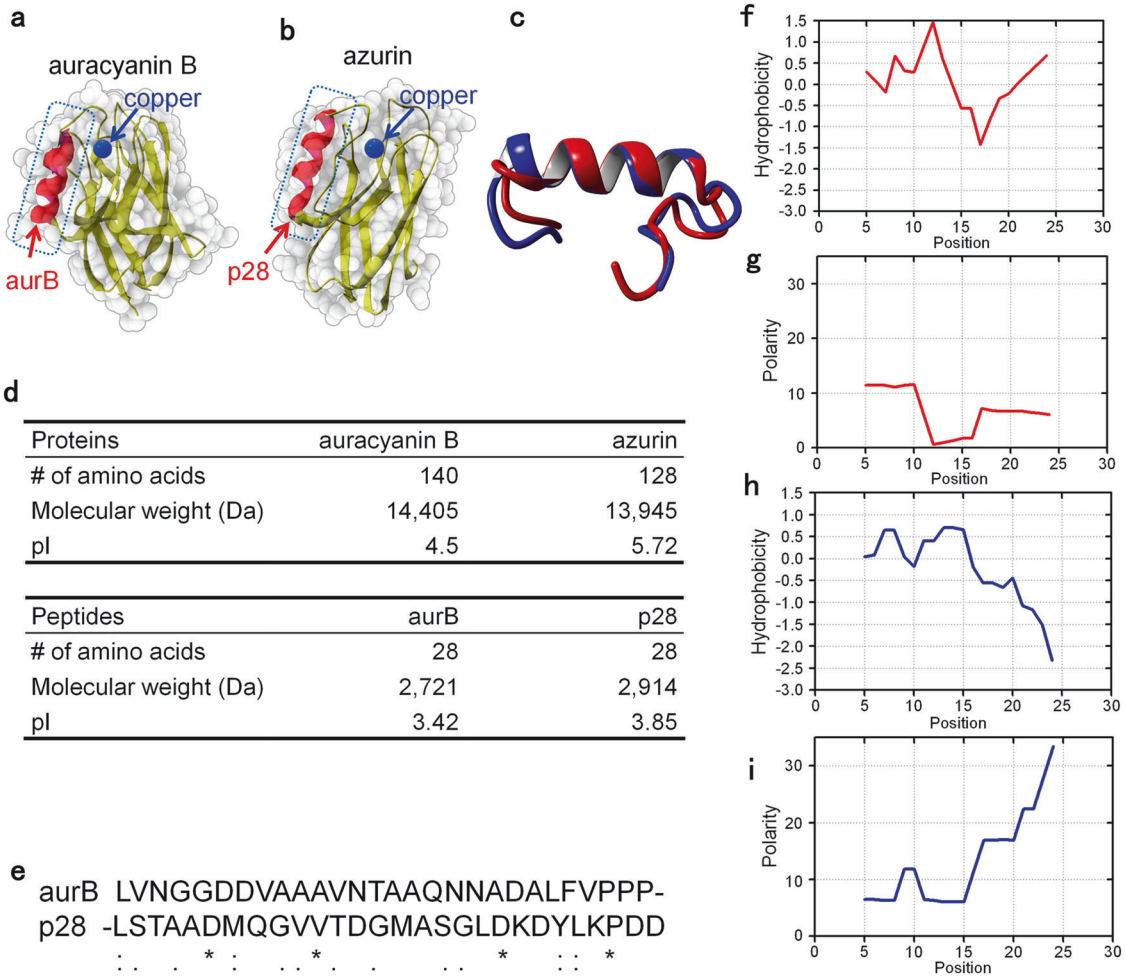

d

Proteins	auracyanin B	azurin
# of amino acids	140	128
Molecular weight (Da)	14,405	13,945
pI	4.5	5.72

Peptides	aurB	p28
# of amino acids	28	28
Molecular weight (Da)	2,721	2,914
pI	3.42	3.85

e

```
aurB  LVNGGDDVAAAVNTAAQNNADALFVPPP-
p28   -LSTAADMQGVVTDGMASGLDKDYLKPDD
          .   * .   .* .     .  *  : .  *
```

Fig. 2 Overall structures of auracyanin B and azurin. Ribbon diagrams and molecular surfaces of each protein (**a**: auracyanin B, **b**: azurin) were visualized by QuteMol and DeepView (Swiss Institute of Bioinformatics). Dotted boxes indicate the locations of the helical (red) peptides aurB and p28. Blue: copper. Structural alignment of aurB (blue) and p28 (red) yields a Cα RMSD of 1.47 Å (**c**). Their molecular weights, numbers of a.a., and pI values are presented. The peptide sequences are described in the "Methods" section (**d**). Multiple sequence alignment with Clustal indicated that a few amino acids were conserved between the two peptides (**e**). "*" represents positions with fully conserved residues. ":" and "." indicate highly conserved substitutions and semiconserved substitutions, respectively. Hydrophobicity plots[41] of aurB (**f**) and p28 (**h**) were generated according to the hydrophobicity scale of Kyte and Doolittle. The polarity scores of aurB (**g**) and p28 (**i**) were calculated according to the polarity propensity scale[100]

a peptide (aurB) from auracyanin B induced dose- and time-dependent apoptosis in human cancer cells in a p53-independent manner, but a peptide from auracyanin A did not exhibit this effect.[43]

Cupredoxin auracyanin B (14.4 kDa, 140 aa) has a molecular core consisting of two β-sandwich domains formed by eight polypeptide strands in a typical cupredoxin fold, similar to the structure of azurin (13.9 kDa, 128 aa) (Fig. 2a–c). Using a similar approach to our p28 studies, we identified a highly water-soluble 28-amino-acid peptide fragment, aurB (residues 61–88 of auracyanin B), derived from its helical motif and possessing a molecular weight of 2,721 Da. Both aurB and p28 are anionic peptides (Fig. 2d); however, sequence alignment revealed that very few amino acids (four out of twenty-eight a.a.) are conserved between aurB and p28 (Fig. 2e). The hydrophobicity plots (Fig. 2f, h) showed that both peptides are amphipathic molecules. The polarity plots (Fig. 2g, i) indicated that the polarity of aurB in the middle to C-terminal region is quite low compared with that of p28, suggesting that the biological functions of these peptides likely vary due to their different chemical characteristics, despite their similar overall structures.

Given that p28 acts via a p53-dependent mechanism in cancer cells, we investigated the antiproliferative effects of aurB on histologically different types of cancer cells with differences in p53 status in vitro. Treatment with aurB significantly decreased the viability of breast cancer (MCF-7), prostate cancer (DU145), and colon cancer (HCT116) cells, regardless of p53 expression status (Supplementary Fig. S2a–c). Moreover, the effects of aurB on p53-inactive cancer cell lines, including PC3 prostate cancer cells, MDD2 breast cancer cells (p53 dominant-negative), and p53-null SKOV3 ovarian cancer, were dose-dependent (Fig. 3a).

Induction of p53 and AR-independent apoptotic cell death

While targeting the androgen receptor (AR) axis has been one of the most successful therapeutic approaches in prostate cancer patients,[44] ~20% of these patients develop castration-resistant prostate cancer (CRPC) within five years of follow-up during androgen deprivation therapy.[45] Prostate cancer is the most common cancer in men and the second leading cause of cancer death in men (after lung cancer) in the United States, which is representative of patterns seen in many Western countries.[46,47] Additionally, current immunotherapies have shown limited efficacy for advanced prostate cancer[6] but are effective for melanoma and lung cancer.[48] Furthermore, prostate cancer models with different p53 statuses have been well established

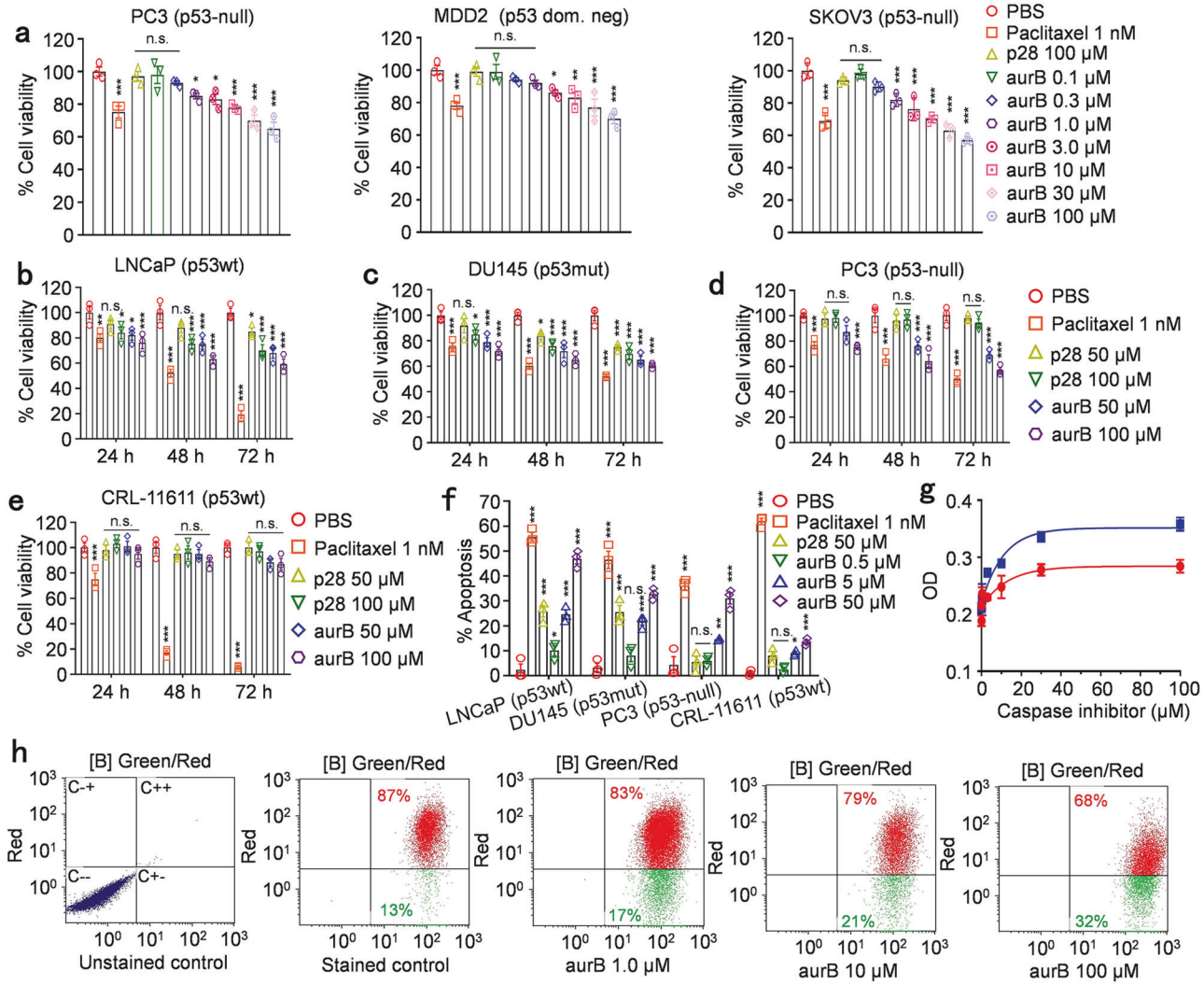

Fig. 3 Effect of peptides on prostate cancer cell lines with differences in p53 and AR expression status. Effect of aurB on p53-null human cancer cells. The dose-dependent effect of aurB on PC3 prostate cancer, MDD2 breast cancer, and SKOV3 ovarian cancer cells was measured by MTT assays (**a**, $N = 3$ for each group). Cell viability assays on prostate cancer cell lines (**b**: LNCaP, **c**: DU145, **d**: PC3, $N = 3$ for each group) and normal prostate cells (**e**: CRL-11611, $N = 3$ for each group) were conducted in the presence of aurB, p28, or paclitaxel. Control (PBS)-treated cells were considered to have 100% viability. Prostate cancer cell lines (LNCaP, DU145, and PC3) and normal prostate CRL-11611 cells were exposed to the indicated agents for 48 h and stained using apoptosis assay kits according to the manufacturer's instructions. The samples were analyzed by flow cytometry (**f**, $N = 3$ for each group). Caspase-3 is involved in aurB-induced apoptosis. The effects of the caspase-3 inhibitor Z-DEVD-FMK on PC3 cells exposed to 100 µM aurB were determined by MTT assays at 24 h (red circle) and 48 h (blue square) (**g**, $N = 3$ for each group). PC3 cancer cells were exposed to aurB at the indicated concentrations. Cells were stained by using JC-1 Mitochondrial Membrane Potential Assay Kits according to the manufacturer's instructions to measure $\Delta\psi_m$, and fluorescence was measured by flow cytometry (**h**). Error bars represent the mean ± SEM. Significant differences were analyzed statistically using ANOVA. n.s., not significant; * $p < 0.05$; ** $p < 0.01$; *** $p < 0.001$

and widely used.[49] After finding that aurB significantly decreased the proliferation of the AR-negative PC3 prostate cancer cell line, we assessed the effects of aurB, p28, and paclitaxel as a positive control (a drug for prostate cancer) on additional prostate cancer cell lines with different molecular signatures. As expected, exposure to paclitaxel significantly induced time-dependent cytotoxicity in the metastatic prostate cancer cell lines LNCaP (derived from left supraclavicular lymph node metastasis, wild-type p53, AR +), DU145 (derived from central nervous system metastasis, heterozygous mutant P223L and V274F p53, AR −) and PC3 (derived from bone metastasis, p53-null, AR −) and the normal prostate cell line CRL-11611 (p53 + , AR +) (Fig. 3b–e). p28 also had a dose-dependent effect on p53-expressing prostate cancer cells (LNCaP and DU145) but not p53-null PC3 cells or normal CRL-11611 cells, confirming our earlier findings.[23,26] Treatment with aurB significantly induced dose-dependent cytotoxic effects on all three prostate cancer cell lines, with a ~50% inhibition rate when aurB was administered at 100 µM for 72 h (Fig. 3b–d). In contrast, aurB did not significantly alter the viability of normal prostate cells (Fig. 3e). Together, these data indicate that the biological functions of these peptides differ due to distinct chemical characteristics, despite structural similarities. While p28 showed a p53-mediated impact on cancer cell viability, aurB significantly reduced cancer viability, regardless of p53 status and AR expression.

We next examined apoptotic cell death in the same set of cell lines exposed to p28, aurB, and paclitaxel by flow cytometry. In all the cell lines, including the normal cells, treatment with paclitaxel induced apoptotic cell death (Fig. 3f). Treatment with p28 induced apoptotic cell death in LNCaP and DU145 cells but not in PC3 cells. Treatment

with aurB significantly increased apoptosis in a dose-dependent manner in all prostate cancer cell lines but had a less extensive effect on normal prostate cells (Fig. 3f). Caspases are essential proteases involved in apoptosis, particularly caspase-3, which is critical for certain apoptotic processes. To determine whether the ability of aurB to induce apoptosis is mediated through caspases, the effects of Z-DEVD-FMK, a cell-permeable inhibitor that irreversibly binds to the catalytic site of caspase-3,[50] were assessed. Treatment with Z-DEVD-FMK decreased aurB-induced cytotoxicity in a dose-dependent manner (Fig. 3g), suggesting that aurB-induced apoptosis occurred through the activation of caspase-3, which is linked to mitochondrial processes (e.g., $\Delta\psi_m$ loss).[51] In fact, aurB exposure induced a dose-dependent increase in the $\Delta\psi_m$ (Fig. 3h). Importantly, although p53 and AR play critical roles in the induction of apoptosis,[52–54] aurB can induce apoptosis in both p53-null and AR-negative cancer cells, suggesting that its mode of action is p53/AR-independent, but it is through the caspase-mediated mitochondrial pathway. Hereafter, we focused on the p53 mutant and AR-negative prostate cancer cell lines DU145 and PC3.

aurB localizes to mitochondria and binds to the ATP synthetase subunit ATP5C

We previously demonstrated that the cupredoxin azurin-derived peptide p28 preferentially enters various types of cancer cells.[24,42,55] Confocal images and flow cytometric analysis (Fig. 4a, b, and Supplementary Fig. S3a, b) showed that aurB preferentially penetrated human prostate cancer cells (DU145: 1.8-fold increase, PC3: 1.7-fold increase over normal prostate cells) without inducing cellular membrane toxicity (Supplementary Fig. S3c). Since aurB induced mitochondria-mediated apoptosis (Fig. 3h), we included normal heart and skeletal muscle cells with high mitochondrial abundances to evaluate aurB cellular entry. As a result, similar to p28, very little aurB cellular entry into normal prostate cell lines (CRL-11611), heart cells (AC16, human cardiomyocytes), and skeletal muscle cells (PSMCs, primary human skeletal muscle cells) were observed (Fig. 4a, b and Supplementary Fig. S3a, b). Moreover, aurB preferentially localized to xenograft tumors in mice (Fig. 4c). Upon entry, aurB colocalized with mitochondria in both DU145 and PC3 prostate cancer cells, whereas AC16 and PSMC cells with high mitochondrial abundances (Fig. 4a, Supplementary Fig. S3d) exhibited minimal peptide uptake (Fig. 4a, b, d), suggesting that aurB cellular entry is mitochondria independent and exerts minimal antiproliferative effects in either cell type (Supplementary Fig. S3e).

To investigate more details of the intracellular localization of aurB upon entry, transmission electron microscopy (TEM) was performed when aurB was conjugated to relatively large nonspherical gold nanorods (GNRs, 25 nm in diameter × 73 nm in length), as GNRs smaller than 15 nm in diameter can enter tumor tissue by themselves.[56] TEM images revealed that GNR-conjugated aurB was clearly internalized by PC3 cells and localized in mitochondria (Fig. 4e). Since aurB is localized in mitochondria, we investigated whether aurB could bind to an endogenous mitochondrial protein(s). For this, pull-down assays with biotin-labeled p28 or aurB were conducted. While aurB pulled down an endogenous mitochondrial protein with a molecular weight of ~35 kDa, p28 did not (Fig. 4f). Mass spectrometry analysis of the 35-kDa protein band and immunoblotting (IB) identified the binding partner of aurB to be the mitochondrial ATP synthase gamma subunit (ATP5C) (Fig. 4g, h). We then determined the affinity of the complex by surface plasmon resonance (SPR). The sensorgram showed a substantial, concentration-dependent increase in the registered response over time when an aurB solution was injected, followed by a relatively small decrease in response when buffer was applied to remove free analyte molecules (Fig. 4i). The specific ATP5C/aurB complex had a long lifetime, with a slow unbinding process (the signal decreased by only ~5% even after 1,200 s of fluxing buffer had been injected). Determination of the ATP5C-aurB binding kinetics showed that the dissociation constant (K_D) (association rate k_{on}: 100 $M^{-1}s^{-1}$ and dissociation rate k_{off}: $4 \pm 2 \times 10^{-5}$ s^{-1}) was 4×10^{-7} M, reflecting a medium-strength interaction under the tested conditions. Fitting with a heterogeneous ligand model slightly improved the simulated sensor gram but largely confirmed the results described above, revealing a minor secondary interaction likely due to ligand heterogeneity.

aurB inhibits ATP production by blocking respiration and glycolysis in mitochondria

Based on the above results, aurB is a promising candidate as a mitochondria-mediated agent for cancer. Thus, we further investigated how aurB affects mitochondrial homeostasis since they play crucial roles in cellular energy metabolism and p53-dependent and p53-independent regulation of programmed cell death.[57–59] Given that ATP5C (ATP5F1C) is a subunit of mitochondrial ATP synthase, we first determined mitochondrial ATP levels by the BioTracker ATP-Red, a red-fluorescent probe for detecting mitochondrial ATP in live cells. The control agent, the ATP synthesis inhibitor oligomycin, decreased the ATP levels in all cell lines tested (Fig. 5a). Treatment with aurB substantially decreased the ATP levels in prostate cancer cells, but lesser effects were observed in normal prostate cells (Fig. 5a). Consistent with these data, ATP synthetase enzyme activity (Complex V, including ATP5C) was significantly inhibited by aurB (Fig. 5b). Furthermore, we characterized key parameters of mitochondrial respiration (OCR: oxygen consumption rate, ATP production rate, and proton leakage) (Fig. 5c–k) and glycolysis ability (Fig. 5l–q) in real time in live cells with the Seahorse XF Mito Stress Test and Glycolytic Stress Test, respectively. Treatment with aurB significantly inhibited the basal and maximal respiratory rates and the spare respiratory capacity in prostate cancer cells, DU145 (Fig. 5c, f) and PC3 (Fig. 5d, g), in a concentration-dependent manner. In sharp contrast, aurB did not significantly inhibit these parameters of mitochondrial respiration in normal prostate cells (Fig. 5e, h). The nonmitochondrial OCR was also significantly inhibited in both cancer cell lines (Fig. 5i, j), potentially due to inefficient mitochondrial electron transport.[60] Importantly, ATP production rates were significantly inhibited by aurB treatment in both DU145 (Fig. 5i) and PC3 (Fig. 5j) prostate cancer cells but not in normal prostate cells (Fig. 5k), consistent with the BioTracker ATP-Red results (Fig. 5a). To compensate for reduced ATP production, cancer cells typically switch from oxidative phosphorylation to glycolysis. However, our results indicate that the extracellular acidification rate (ECAR), glycolysis, glycolytic capacity, and glycolytic reserve were also suppressed in DU145 (Fig. 5l, o) and PC3 (Fig. 5m, p) prostate cancer cells, unlike normal prostate cells (Fig. 5n, q), treated with aurB in a dose-dependent manner, suggesting that the glycolytic pathway was also significantly blocked by aurB. These data support the results described earlier. Proton leakage, which leads to uncoupled respiration, refers to the migration of protons into the mitochondrial matrix without the complete production of ATP. Together, these results demonstrated that aurB preferentially enters cancer cells, localizes to mitochondria, and binds to mitochondrial ATP5C, which leads to inhibition of energy production, mitochondrial swelling, and $\Delta\psi m$ loss. These cascades induce apoptotic cell death in prostate cancer cells independent of p53 and AR.

Inhibition of tumor growth by aurB in prostate cancer animal models

First, we performed a biodistribution assay using IRDye800CW-labeled aurB to determine the in vivo stability of aurB in a prostate cancer animal model (Supplementary Fig. S4). By 48 h, IRDye800CW-aurB signals were largely cleared from systemic circulation, with only minimal retention observed in the kidney (Supplementary Fig. S4a). In addition, the half-life of aurB based on intensity was 21.2 h, compared with 8.1 h for IRDye800CW alone

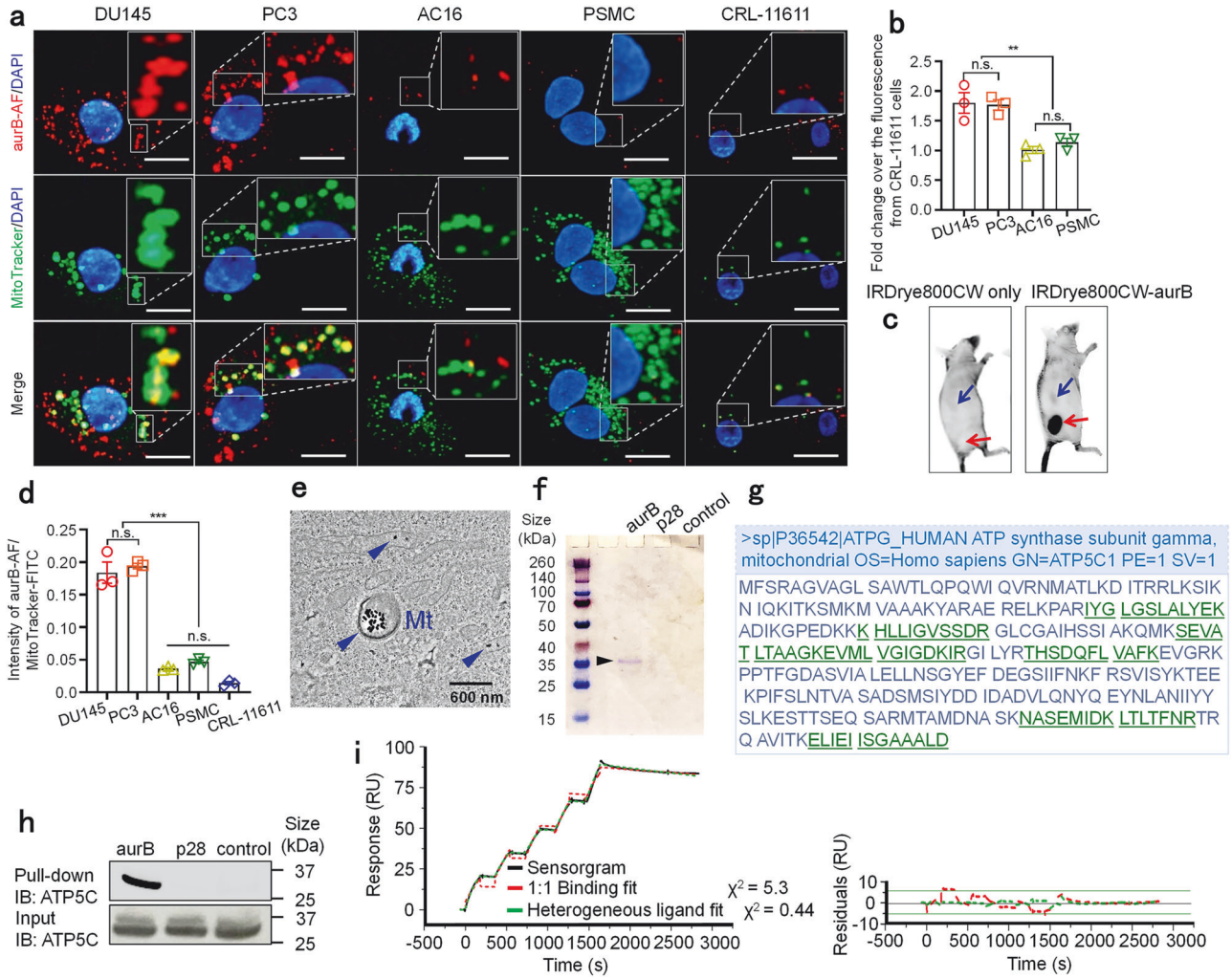

Fig. 4 aurB preferentially enters cancer cells, localizes to mitochondria, and binds to ATP5C. Confocal microscopy analysis of Alexa Fluor-labeled aurB (aurB-AF) and MitoTracker uptake by DU145, PC3, AC16, PSMC, and CRL-11611 cells (**a**). Red: Alexa Fluor-labeled aurB; Green: MitoTracker; Blue: Nucleus. Scale bar: 20 μm. Each panel on the right side includes the image at higher magnification of the boxed region under each panel. The intensity of aurB-AF was quantified by flow cytometry, and the fold-increase over fluorescence from normal prostate cells was calculated (**b**, $N = 3$ for each group). Images of IRDye800CW only and IRDye800CW-aurB in PC3 xenograft mice. PC3 cells were injected subcutaneously, and once tumors reached ~50 mm^3, IRDye800CW only and IRDye800CW–aurB were administered intravenously. Forty-eight hours post-injection, the mice were imaged with an Odyssey scanner. Kidneys (blue arrows) show signals from dye excretion; tumors are indicated by red arrows (**c**, $N = 5$ for each group). The intensity of aurB-AF and MitoTracker-FITC was quantified by flow cytometry, and the ratio of intensity of aurB-AF/MitoTracker-FITC was calculated (**d**, $N = 3$ for each group). Representative TEM micrograph of aurB-treated cells depicting the intramitochondrial localization of aurB-GNRs (blue arrowheads) and mitochondrial (Mt) swelling. Scale bar: 600 nm. Mt: mitochondria (**e**). Identification of aurB binding protein (**f–h**). The mitochondrial fractions of PC3 cells were incubated with biotin-labeled p28 or aurB. Coomassie-stained SDS–PAGE gels are shown (**f**). The protein band at ~35 kDa (black arrowhead) was identified as ATP5C using mass spectrometry analysis. The identified fragments are indicated in the green underlined sequence (**g**). IB with an anti-ATP5C antibody confirmed that aurB physically binds to ATP5C (**h**). Binding kinetics of ATP5C and aurB (**i**). Top: SPR sensorgram (black solid curve) of a representative single-cycle kinetics assay performed at 298 K by the injection of five increasing concentrations (187, 281, 421, 632, 947 μM) of aurB in running buffer over the sensorchip surface functionalized with ATP5C; global fit (dashed curves) of the sensorgram according to the Langmuir 1:1 binding model (red curve) and the heterogeneous ligand model (green curve) together with the corresponding χ^2 values. Bottom: Fit residuals. Error bars represent the mean ± SEM. Significant differences were analyzed statistically using ANOVA. n.s., not significant; ** $p < 0.01$; *** $p < 0.001$

(Supplementary Fig. S4b). Notably, IRDye800CW-aurB signals continued to accumulate in the tumor sites and were detectable at the tumor sites up to 72 h post-injection (Supplementary Fig. S4b, c). In contrast to the IRDye800CW alone group, significant contrast between the tumor and the surrounding normal tissues was detected at 24–72 h following the injection of IRDye800CW-aurB (Supplementary Fig. S4b, c). These findings indicate that aurB was preferentially localized at the tumor sites and retained for several days after systemic injection in this preclinical setting. These data encouraged us to investigate whether the effects of aurB observed in vitro translate in vivo, mouse xenograft models were used (Fig. 6a). In mice bearing PC3 xenograft tumors, aurB significantly inhibited the growth of PC3 tumors over the course of four weeks of treatment (Fig. 6b, $p < 0.05$) without inducing either behavioral changes or a decrease in body weight (Fig. 6c). At the end of the treatment period, aurB and paclitaxel inhibited tumor growth by ~65% and 52% (vs. the PBS control), respectively. These results are consistent with the in vivo findings above. In an aggressive p53-null, AR-negative neuroendocrine prostate cancer model, aurB exhibited significant antitumor activity without

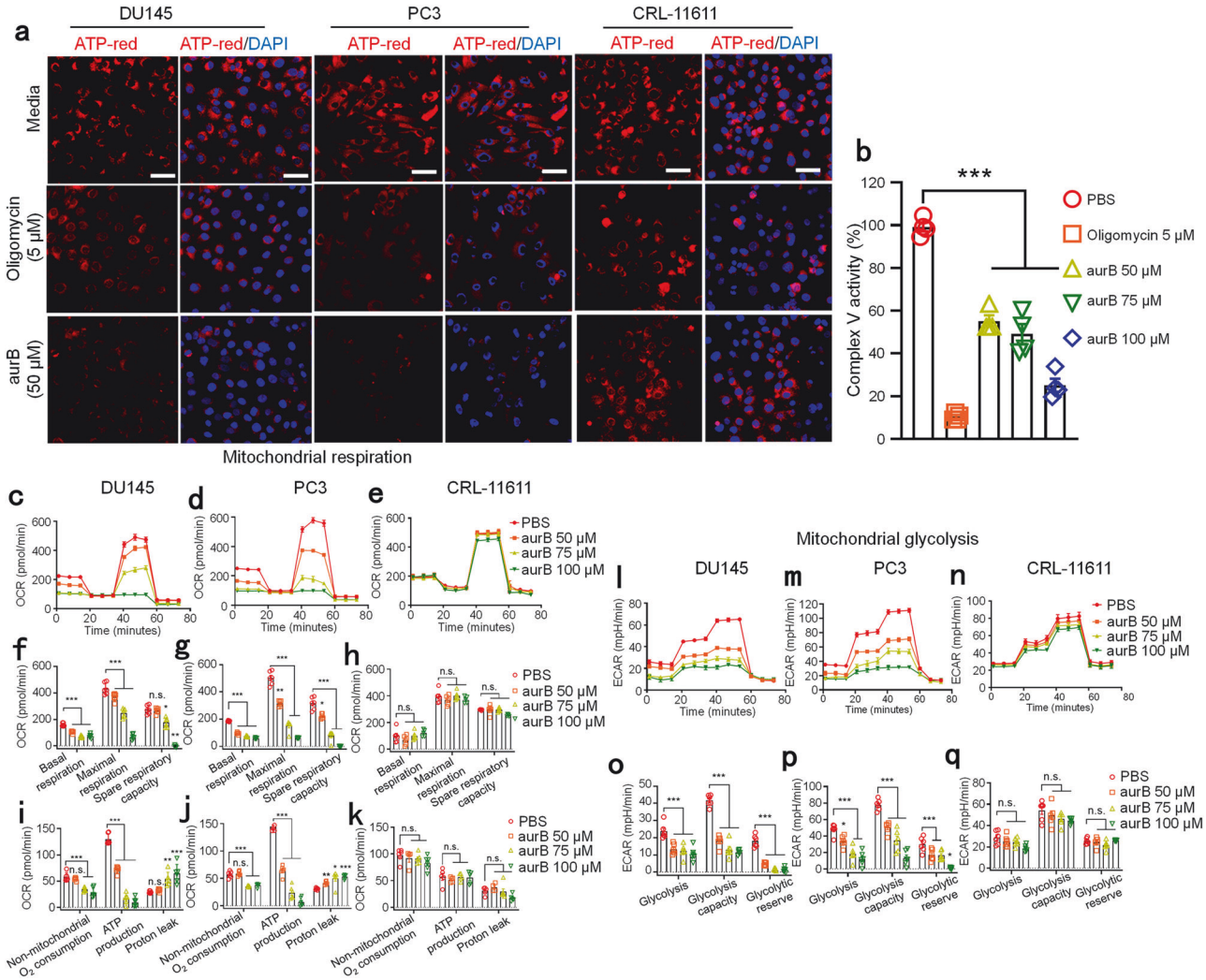

Fig. 5 aurB inhibits ATP synthesis. Intracellular ATP in prostate cancer cells (DU145 and PC3) and normal cells (CRL-11611) (**a**). Cells were incubated with oligomycin (5 μM) and aurB (50 μM) for 24 h. Live cells were stained with ATP-Red (10 μM for 15 min) and subsequently treated with DAPI (1 μM for 15 min). Red: ATP-Red; blue: DAPI. Scale bar: 50 μm. The mitochondrial fractions from prostate cancer cells were treated with various concentrations of aurB (50 μM, 75 μM, and 100 μM), 5 μM oligomycin, or PBS, and the Complex V activity was analyzed using an ATP synthase enzyme activity microplate assay kit (**b**, $N = 4$ for each group). Seahorse assay data showed real-time changes in the oxygen consumption rate (OCR), nonmitochondrial oxygen consumption, ATP production, proton leakage (**c–k**), extracellular acidification rate (ECAR), glycolysis, glycolytic capacity, and glycolytic reserve (**l–q**) in prostate cancer cells (DU145, PC3) and normal cells (CRL-11611) following treatment with different concentrations of aurB ($N = 6$ for each group). Error bars represent the mean ± SEM. Significant differences were analyzed statistically using ANOVA. n.s., not significant; * $p < 0.05$; ** $p < 0.01$; *** $p < 0.001$

apparent adverse events. In contrast, p28 did not inhibit the growth of PC3 (p53-null) xenografts, consistent with the in vitro data (Fig. 3a, d, f). In addition, aurB significantly decreased tumor weight (Fig. 6d), which was consistent with the tumor growth data. Histological analyses of the tumors revealed that proliferating cells (Ki-67 positive) were randomly distributed among the tumor parenchyma of control animals (Fig. 6e). In contrast, aurB treatment substantially reduced the number of Ki-67-positive proliferating cells (Fig. 6e). Given the importance of apoptosis in the in vitro effects of aurB, we next aimed to assess the apoptotic effect of aurB in vivo by performing TUNEL assays and caspase-3 staining on xenograft tumor samples. Although the tumors of control animals contained few TUNEL-positive apoptotic cells, the tumors of aurB-treated animals contained more apoptotic cells (Fig. 6f). Furthermore, a substantial increase in the proportion of caspase-3-positive cancer cells was found in the tumors of aurB-treated animals compared with those of control animals (Fig. 6g), indicating that aurB suppresses tumor growth by inducing caspase-mediated apoptosis.

Next, we studied the effects of aurB in a metastatic prostate cancer mouse model consistent with the cell lines from which the in vitro data were obtained (Fig. 7a). The most common metastatic site of prostate cancer is the bones, and ~90% of men who die from prostate cancer have metastatic disease in their bones.[46,61] Because resistance to radiation therapy, a key treatment for patients with metastatic prostate cancer, is related to mitochondrial energy production,[62] and as aurB was found to inhibit ATP generation, we hypothesized that aurB would act synergistically with radiation therapy to improve treatment efficacy. First, we conducted a synergy assay to confirm the synergistic effect of irradiation therapy and aurB in vitro. As shown in Supplementary Fig. S5a, the calculated synergy score for the combination of irradiation and aurB was 10.18, indicating a synergistic interaction between the two treatments. To clarify this hypothesis in a preclinical context, we used a well-established animal model generated via intratibial injection.[63] Consistent with the effects of aurB in the primary tumor model (Fig. 6), aurB administered alone significantly inhibited (68% reduction at week 5 vs. the PBS

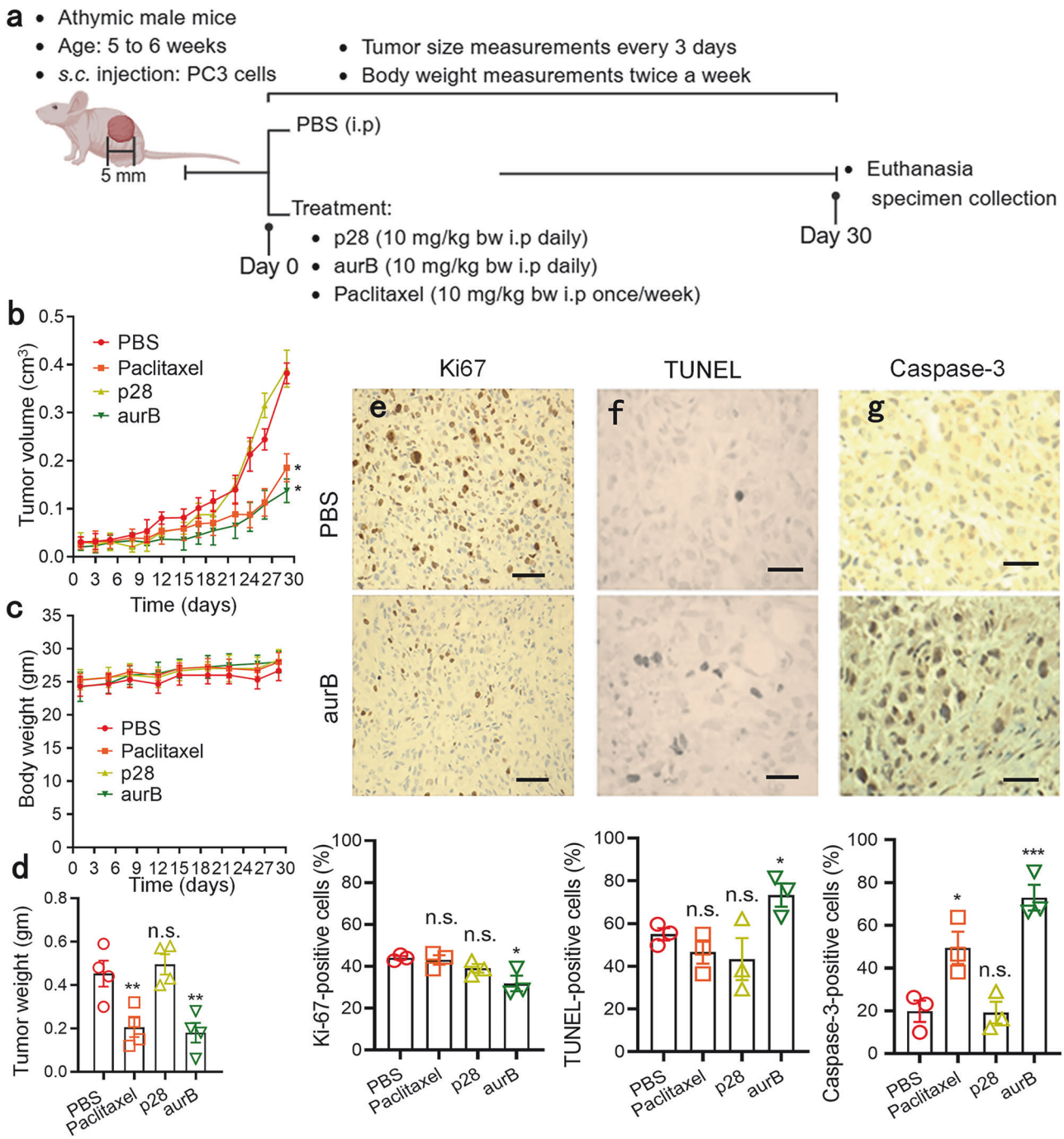

Fig. 6 aurB inhibits PC3 xenograft tumor growth. Schematic representation outlining the in vivo study (**a**, Created in BioRender, https://BioRender.com). When the *s.c.* tumors reached ~5 mm, athymic mice were randomized into control (PBS) and *i.p.* treatment groups (**b**, $N = 5$ for each group). None of the treatments significantly altered the body weight of the animals (**c**). At the end of treatment, tumors were dissected and weighed (**d**). In sections of tumors from the control group, there was a marked increase in Ki-67-positive proliferating cells (**e**, stained brown), and only a few apoptotic cells were observed, as determined by TUNEL (**f**) and caspase-3 (**g**) staining. There was an apparent sharp reduction in Ki67-positive proliferating cells and a higher number of TUNEL-positive apoptotic cells in the aurB-treated group than in the control group ($N = 3$ for each group). Similarly, caspase-3 expression in aurB-treated tumors was markedly increased compared with that in untreated controls ($N = 3$ for each group). Scale bar: 100 µm. Error bars represent the mean ± SEM. Significant differences were analyzed statistically using ANOVA. n.s., not significant; * $p < 0.05$, ** $p < 0.01$, *** $p < 0.001$

control, $p < 0.001$) tumor growth in the tibia (Fig. 7b, c) without inducing either behavioral changes or a decrease in body weight (Fig. 7d). As expected, radiation therapy alone significantly inhibited tumor growth (vs. the PBS control, $p < 0.001$). More importantly, tumor growth in the animals treated with aurB in combination with radiation therapy was significantly lower than that in animals treated with aurB or radiation therapy alone, and combination treatment was not accompanied by a decrease in body weight. Compared with the PBS control group, combined treatment with aurB and radiation therapy significantly decreased tumor growth by 99% at week 5. Magnetic resonance imaging (MRI) at week 5 and images of the tibial bones clearly revealed

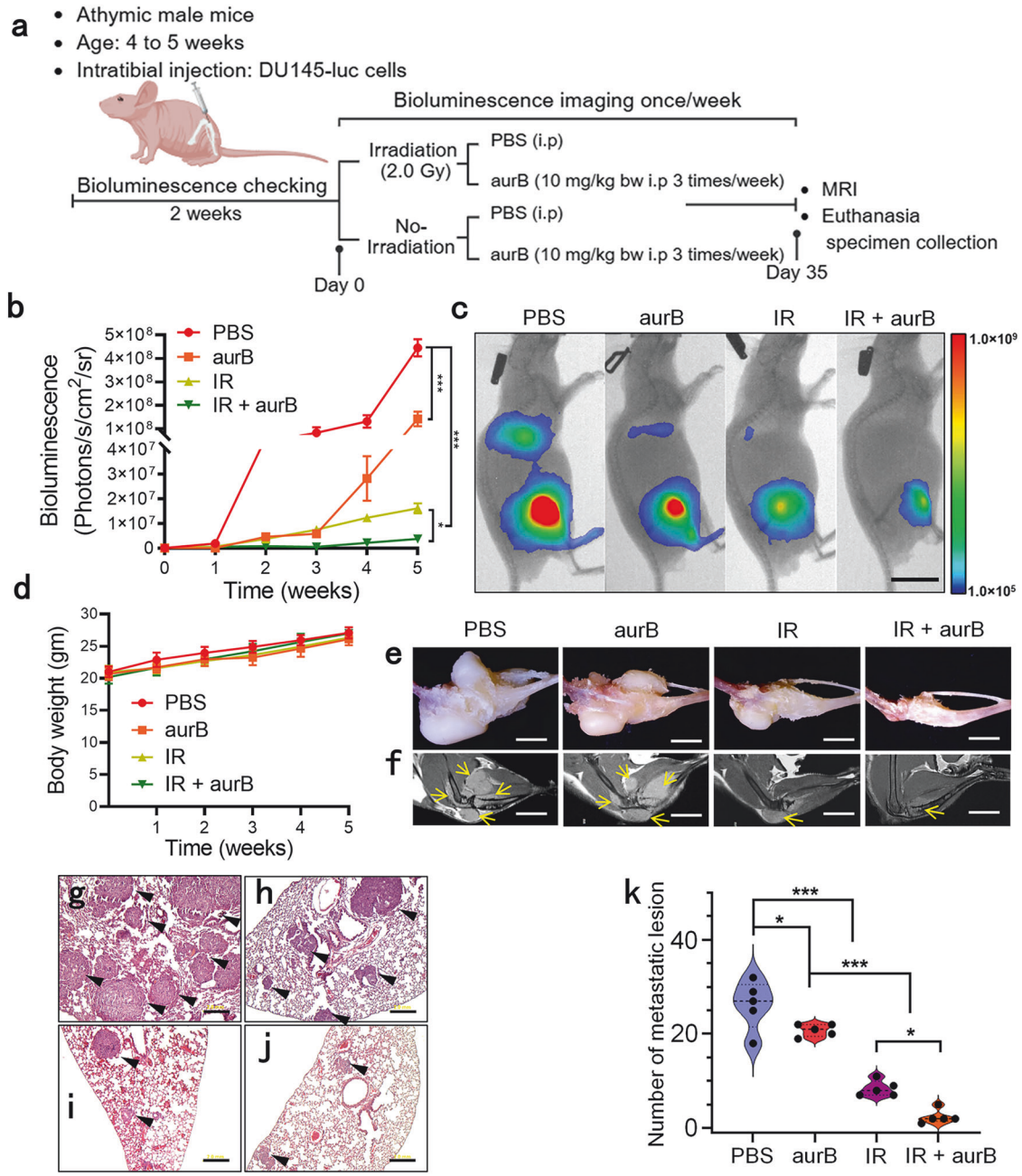

Fig. 7 aurB prevents bone metastasis in the DU145 prostate cancer model. Schematic representation outlining the bone metastasis animal model (**a**, Created in BioRender, https://BioRender.com). Quantification of the luciferase signal from DU145-luc cells in mice treated with PBS, aurB (10 mg/kg), IR (2.0 Gy), or a combination of aurB (10 mg/kg) and IR (2.0 Gy) (**b**, $N = 5$ in each group). Representative bioluminescent images of tumor growth in the tibia at 5 weeks (**c**, scale bar: 2.5 cm). Lung metastases were detected. None of the treatments significantly altered the body weight of the animals (**d**). Representative photo images (**e**) and MRI scans (**f**) of prostate tumors in the tibia at the end of treatment (5 weeks, scale bar: 0.5 mm). Yellow arrows indicate tumors. Representative H&E staining images of lung tissues after mice were sacrificed at 5 weeks: PBS (**g**), aurB 10 mg/kg (**h**), IR 2.0 Gy (**i**), and aurB 10 mg/kg in combination with IR 2.0 Gy (**j**). Scale bar: 2 mm. The number of metastatic lesions in the lung was analyzed by ImageJ (**k**). Error bars represent the mean ± SEM. Significant differences were analyzed statistically using ANOVA. n.s., not significant; * $p < 0.05$; *** $p < 0.001$

that aurB enhanced the antitumor activity of radiation therapy (Fig. 7e, f).

As DU145 cells are highly metastatic prostate cancer cells, we also evaluated the number of metastatic lesions in other major organs of the mice in each group. Metastatic lesions were found only in the lungs (Fig. 7g–j) and not in the heart, spleen, liver, or kidney (Supplementary Fig. S5b). Consistent with the observed antitumor effects of aurB (Fig. 7b), treatment with aurB alone significantly reduced (21% reduction at week 5 vs. the PBS control, $p < 0.05$) the number of metastatic lesions in the lungs (Fig. 7g, h, k). Radiation therapy alone also reduced (68% reduction vs. the PBS control, $p < 0.001$) the number of metastatic lesions in the lungs (Fig. 7g, i, k), but more notably, the number of metastatic lesions in the combination group was significantly lower (91% reduction, vs. the PBS control) than that in the groups treated with aurB or radiation therapy alone (Fig. 7g–j, k). Together, aurB enhanced the effectiveness of radiation therapy by inhibiting ATP generation, which is crucial because resistance to radiation

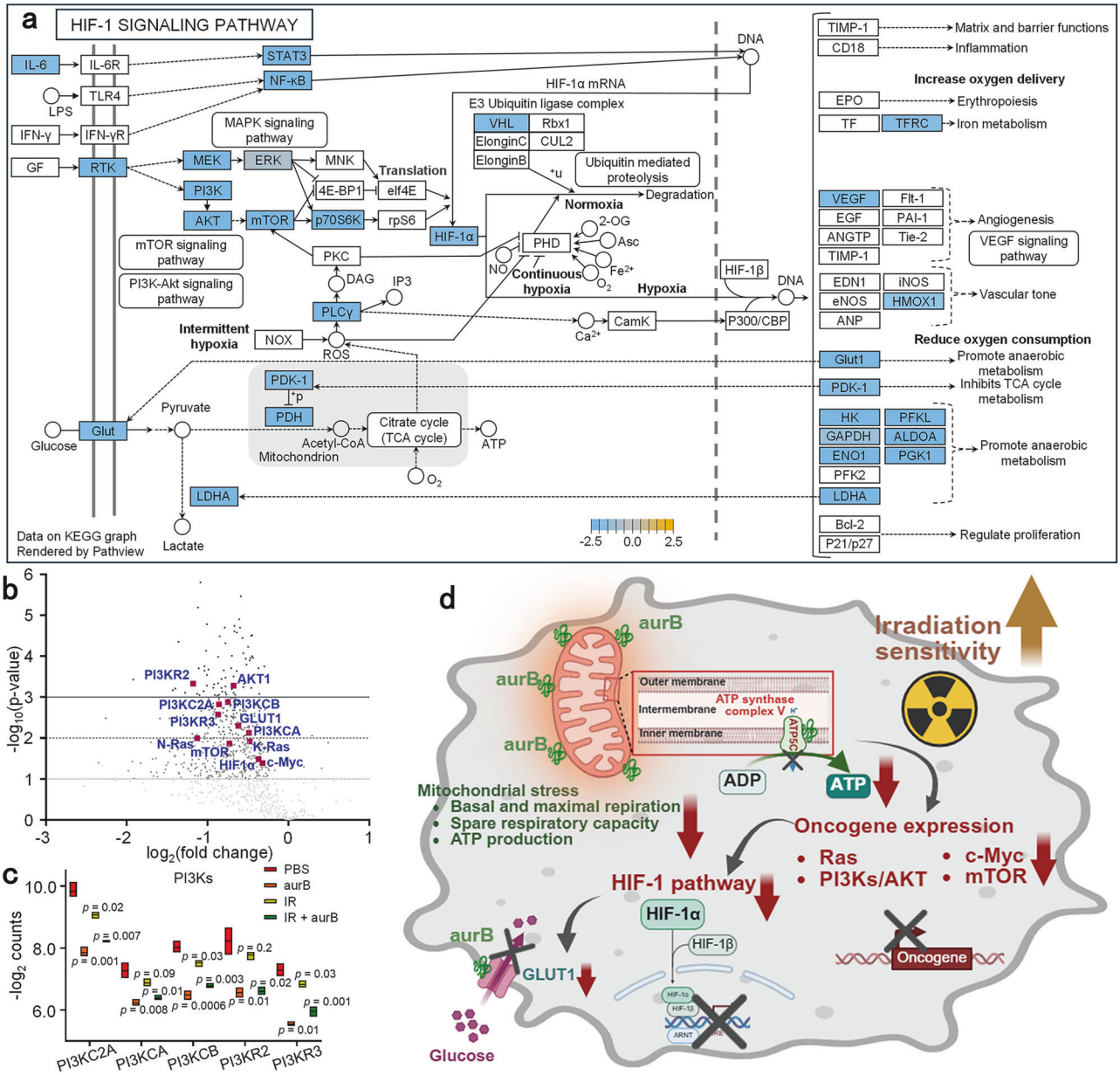

Fig. 8 Multiplex RNA expression profiling with an nCounter analysis. Pathview analysis, performed using NanoString nSolver software, presents a comprehensive pathway map for differentially expressed genes (aurB vs. PBS) within the HIF-1 signaling pathway (**a**). Gene expression levels are indicated as significantly higher (gold), unchanged (gray), or lower (blue) in aurB-treated vs PBS. A volcano plot (Combination: IR 2.0 Gy + aurB 10 mg/kg vs. IR) shows each tested gene, plotted by comparing $-\log_{10}$ (p value) with $\log_2$-fold change. Horizontal lines represent statistical significance, with highly significant values appearing at the top of the plot, while highly differentially expressed genes are positioned at the horizontal extremes (**b**). Highlights the downregulation of the PI3K genes in the various treatment groups (**c**). Schematic representation of the aurB-induced pathway in cancer cells (**d**, created in BioRender, https://BioRender.com). ATP production is inhibited by aurB by binding to ATP5C. This induces H^+ leakage and inhibition of respiration in mitochondria. Variations in the status of oncogenes and hypoxia are important triggers of HIF-1α. As a transcription factor, HIF-1α regulates the expression of various genes involved in radiation resistance. Inhibiting ATP production via aurB enhanced radiation sensitivity by modulating multiple pathways through HIF-1α

therapy in metastatic prostate cancer patients is linked to mitochondrial energy production.

aurB enhances radiation sensitivity in tumors via the HIF-1 pathway

To further investigate the underlying molecular mechanisms, we determined RNA expression in these tumor samples via multiplex RNA expression profiling with an nCounter analysis system. KEGG pathway analysis of the differentially expressed genes in the aurB-treated group compared with the PBS-treated group revealed that the HIF-1 pathway was significantly enriched in the genes whose expression was downregulated in the aurB group compared with the PBS group (Fig. 8a). In contrast, radiation therapy (IR) alone did not downregulate the HIF-1 pathway (Supplementary Fig. S6a). Importantly, aurB treatment in combination with IR significantly downregulated genes in the HIF-1 pathway compared with their expression in the IR group, suggesting that the downregulation of these genes was due to the effect of aurB (Fig. 8b, Supplementary Fig. S6b).

The hypoxic microenvironment of the tumor presents a major obstacle for radiation therapy and decreases its effectiveness.[64] HIF-

1α is regulated by the PI3K/mTOR pathway.[65] Thus, to further investigate the alteration of gene expression in the pathway, we analyzed phosphoinositide 3-kinase (PI3K) genes in each treatment. Under ATP-limiting conditions established via aurB treatment, PI3K expression was significantly decreased in the groups treated with aurB alone and with aurB in combination with IR (Fig. 8c). HIFs can interact with proto-oncogenes, such as c-Myc, altering tumor metabolism and proliferation.[65] The interaction of HIF-1 and c-Myc directs cancer cells toward glycolysis by increasing glucose transporter-1 (GLUT-1)-induced radioresistance.[65–67] Because HIF-1 was downregulated by aurB, GLUT-1 was also significantly downregulated by aurB treatment (Supplementary Fig. S6c), and the glycolysis pathway (anaerobic metabolism) was inhibited in the aurB and combination treatment groups (Fig. ca, Supplementary Fig. S6b) but not in the IR group (Supplementary Fig. S6a). As a transcription factor, HIF-1α regulates the expression of dozens of genes involved in maintaining homeostasis.[66] HIF-1α confers radiation resistance in cancer cells via multiple pathways.[65] Taken together, our results suggest that the inhibition of ATP production by aurB through both oxidative phosphorylation and glycolysis increases sensitivity to radiation via the modulation of multiple pathways through HIF-1α (Fig. 8d).

DISCUSSION

In this study, we demonstrated the antiproliferative activity of aurB in various histological types of human cancer cells, including a set of prostate cancer cell lines widely used in therapeutic research.[63] Importantly, aurB was effective against p53-WT, p53-mutant, and p53-null cell lines. The fact that the tumor suppressor p53 is the most frequently mutated gene in cancer[62] and that p53 mutations typically alter p53 activity (depending on the exact mutation sites)[68,69] indicates that p53 is a relevant therapeutic target for cancer drug development. There have been intense efforts to target mutant p53 reactivation in cancer, and several compounds that do so have been identified.[26,70] However, this promising approach does not apply to p53-null cancer cells, suggesting that different therapeutic strategies to treat p53-null cancer cells are needed. Moreover, p53-null PC3 cells, but not LNCaP cells, are considered small-cell neuroendocrine carcinoma cells[71] that do not form glands and are negative for AR and prostate-specific antigen (PSA).[72] Neuroendocrine prostate cancer is extremely aggressive, does not respond to hormonal therapy very well and is characterized by a relatively 'cold' tumor immune microenvironment, similar to other metastatic prostate cancers.[73] Since the five-year survival rate of patients with metastatic and advanced prostate cancer in the US is 31%, as opposed to nearly 100% for patients with local prostate cancer,[74] a new therapeutic option needs to be developed to improve the survival of patients with metastatic and advanced prostate cancer. In this study, we compared the effects of aurB and p28 with those of paclitaxel, which is among the current chemotherapeutic agents for prostate, breast, and ovarian cancer.[75,76] Paclitaxel was most toxic to the normal prostate cell line (CRL-11611), and p53-mutant cell lines (DU145 and PC3) were less susceptible to paclitaxel treatment than were p53 wild-type and androgen-sensitive LNCaP cells. In contrast, all three prostate cancer cell lines tested were more sensitive to aurB than the normal prostate cell line. The results also confirmed that the antiproliferative effects were significantly greater in prostate cancer cells than in their normal counterparts and normal cells (AC16 and PSMC) having high levels of mitochondria content after treatment with aurB. The cellular entry of aurB is mitochondria-independent, and preferential entry was demonstrated in vitro as well as in vivo, thereby making aurB effective in such cancer cells. A substantial proportion of the reported cell-penetrating peptides (CPPs), such as TAT and octamer arginine, are cationic. Given that cellular membranes are generally negatively charged (e.g., phospholipid head groups), these cationic CPPs can have electrostatic interactions with the membrane.[77,78] Unlike cationic CPPs, both aurB and p28 are anionic and amphipathic CPPs (Fig. 2). We previously demonstrated that the secondary structure of p28 (e.g., α-helix/β-sheet motifs) was important for its entry.[25] Additionally, several CPPs can alter their cellular entry by modulating membrane permeability in cancer cells.[79,80] Although the mode of entry for aurB remains unknown, its preferential entry is of considerable significance, motivating our commitment to an in-depth investigation of its mechanism.

Upon entry, aurB induces the downregulation of oncogenes by limiting mitochondrial energy production. Recent studies have shown that high mitochondrial ATP production contributes to cancer drug resistance and metastatic potential.[81,82] ATP-high cancer cells were generally aggressive, exhibiting multidrug resistance and an increased capacity for cell migration/invasion and metastasis. For example, cancer metastasis was largely prevented by treatment with Bedaquiline, which binds to and inhibits mitochondrial ATP synthase, leading to ATP depletion. Bedaquiline is an antibiotic for tuberculosis, and interestingly, using the chick embryo metastasis assay, it was found to significantly suppress spontaneous metastasis (>90 μM) without tumor growth inhibition.[83] This supports our approach that targeting the ATP synthase enzyme presents a compelling avenue for cancer therapy by inhibiting mitochondrial energy production, which in turn weakens the proliferation and metastatic potential of aggressive cancer cells.

In conclusion, we identified a novel aurB derived from a bacterial electron transfer protein that blocks ATP production by targeting a mitochondrial enzyme and induces caspase-mediated apoptotic cancer cell death, demonstrating its potential therapeutic value. Mitochondria in cancer cells are structurally and functionally different from those in normal cells, generally.[84,85] Many conventional agents target signaling pathways that lie upstream of mitochondria and converge on these organelles to induce cell death,[86] suggesting that the development of potential anticancer agents that directly target the energy production machinery in mitochondria is a logical approach. In general, the mitochondrial mass is greater in carcinoma tissues than in benign prostate tissues of all Gleason grades[87], and high levels of mitochondrial ATP synthase Complex V components, including ATP5C, are a significant risk factor in cancer,[3,4,88,89] suggesting that mitochondrial ATP synthase Complex V is a promising druggable target (Supplementary Fig. S7a, b). To our knowledge, this is the first study to show that photosynthetic bacterial proteins can be important sources for the development of immune-independent drugs that directly target the mitochondrial energy production system. Mitochondria play a critical role in energy production and the regulation of cell death in eukaryotic cells and are believed to have originated from ancient bacteria. In this study, our findings indicate that a peptide derived from a bacterial protein may serve as a promising therapeutic candidate for advanced prostate cancer. Building on this concept and acknowledging the limited number of tumor samples analyzed, future investigations could expand the search for mitochondria-targeting peptides of bacterial origin through larger screening approaches. Given that mitochondrial ATP synthetase is often upregulated in several types of cancers, especially prostate cancer, breast cancer, ovarian cancer, glioblastoma, and clear cell renal cell carcinoma,[90] this study could be an important reference for the development of novel peptide-based agents that modulate mitochondrial homeostasis.

MATERIALS AND METHODS

Peptide synthesis

Peptides were chemically synthesized (CS Bio and CPC Scientific, CA) at >95% purity and mass balance. The sequences were as follows: aurB (auracyanin B aa 61–88): LVN GGD DVA AAV NTA

AQN NAD ALF VPPP, and p28 (azurin aa 50-77): LST AAD MQG VVT DGM ASG LDK DYL KPDD. These amino acids are all L-isomers without chemical modification unless otherwise specified.

aurB and p28 labeling

Fluorescence conjugation was performed as described previously.[42] Briefly, aurB or p28 was dissolved in PBS (pH 7) mixed with Alexa Fluor 568 dye (Invitrogen, MA) at a 1:2 peptide/dye ratio. Sodium bicarbonate (pH 8.5) was added and incubated at 4 °C with continuous stirring in the dark. For IRDye conjugation, aurB was dissolved in PBS and reacted with IRDye800CW (LICORbio, NE) in anhydrous DMSO for 3 h at room temperature in the dark. IRDye800CW-labeled aurB, Alexa Fluor 568-labeled aurB, and p28 were dialyzed against cold PBS using Slide-A-Lyzer Dialysis Cassettes (Pierce Biotechnology, IL).

Cell lines and culture

Human cancer and noncancer (immortalized and nonimmortalized) cell lines were obtained from the American Type Culture Collection prostate cancer (PC3, DU145, and LNCaP), normal prostate (CRL11611), breast cancer (MCF-7), ovarian cancer (SKOV3), lung cancer (A549), colon cancer (HCT116), normal human cardiomyocytes (AC16 human cardiomyocytes, CRL-3568), and skeletal muscle cells (primary human skeletal muscle cells—PSMCs, PCS-950-010). MDD2 breast cancer cells (p53 dominant-negative) were provided courtesy of Dr Andrei V. Gudkov, Roswell Park Cancer Institute.[24] All cell lines, except for AC16 and PSMC, were cultured in MEM-E (Invitrogen, MA) supplemented with 10% heat-inactivated fetal bovine serum (Atlanta Biological, GA), 100 units/ml penicillin, and 100 µg/ml streptomycin at 37 °C in 5% CO_2. The human melanoma (UISO-Mel2) cell line was established by our laboratory.[91,92] For AC16 cells, the growth medium consisted of DMEM/F12 supplemented with 12.5% FBS. To induce differentiation, the cells were cultured in DMEM/F12 supplemented with 1× ITS and 2% horse serum. For PSMCs, cells were cultured in DMEM supplemented with L-glutamine (2 mM) and 20% FBS. To induce differentiation, PSMCs were cultured in DMEM with 2% horse serum, 10 µg/ml insulin, 5.5 µg/ml transferrin, and 1 mM sodium pyruvate.

Cytotoxicity assay

The proliferation assay was performed as we previously described.[42] Briefly, cells were cultured in 96-well plates overnight and subsequently treated with the indicated agents for 24, 48, and 72 h at 37 °C in a 5% CO_2 atmosphere.

Flow cytometric analyses

Three prostate cancer cell lines and a normal cell line were treated with paclitaxel at 1 nM, p28 at 50 µM, and aurB at 0.5–50 µM. After 48 h, annexin-V apoptosis assays (Thermo Fisher, MA) were conducted to detect apoptotic cells. For mitochondrial intensity analysis, cells were seeded in petri dishes. After overnight culture, the cells were washed with PBS and incubated with 20 µM Alexa Fluor 568-labeled aurB for 2 h at 37 °C. Then, the cells were treated with 200 nM MitoTracker Green (M7514, Thermo Fisher, MA) for 30 min. At least 10,000 cells in each case were analyzed by FACS (RRC, UIC). JC-1 dye (Invitrogen, MA) was used to determine $\Delta\psi_m$. PC3 cells were exposed to 1, 10, and 100 µM aurB. After washing with PBS, trypsinized PC3 cells were incubated with JC-1 dye and analyzed by FACS.

Caspase assay

Similar to the procedure for the proliferation assays, PC3 cells were exposed to aurB in the presence or absence of the specific caspase inhibitor Z-DEVD-FMK.

TEM

Gold and peptide conjugations were carried out as we previously described.[37] Gold nanorods (GNRs; Nanopartz Inc., CO) were conjugated to peptides following the supplier's protocol. Briefly, NHS-functionalized nonspherical GNRs (25 nm diameter × 73 nm length) were reacted with aurB at a 500-fold molar excess in 0.1 M borate buffer (pH 8.0) for 4 h at room temperature. After conjugation, the peptide-labeled GNRs were washed in 1% PBS containing 0.1% Tween 20 by centrifugation at 9000 rcf for 10 min and then resuspended in PBS. For ultrastructural analysis, PC3 cells were incubated with aurB-GNRs at 300 µg/ml for 16 h. Cell culture samples of ~1 mm^3 were fixed in 4% phosphate-buffered glutaraldehyde and subsequently rinsed with 2% sucrose prepared in 0.1 M Sorensen's phosphate buffer at room temperature. The samples were then post-fixed in 1% osmium tetroxide in 0.1 M Sorensen's phosphate buffer for 1 h at room temperature. Following washes in distilled water, specimens were dehydrated in acetone and infiltrated with EMBed 812 resin (EMS) using a graded acetone-to-resin series consisting of 30 min in 2:1 acetone:resin, 30 min in 1:1 acetone:resin, 1 h in 1:2 acetone:resin, and 1.5 h in 100% resin. Samples were embedded in molds and polymerized overnight at 60 °C. Ultrathin sections (60 nm) were cut with an ultramicrotome, mounted on 200-mesh copper grids, stained with uranyl acetate and lead citrate, and examined using a Philips CM 120 transmission electron microscope.

Pull-down assay, protein identification, and western blot analysis

Cells were washed twice with PBS, and the mitochondrial fraction was prepared with the Qproteome Mitochondria Isolation Kits (Qiagen, MD). Mitochondrial proteins were extracted with 10% n-dodecyl-β-D-maltoside (Mitochondrial Protein Immunoprecipitation kits, Sigma, MA) and incubated with biotin-labeled p28 or biotin-labeled aurB for 16 h at 4 °C. Streptavidin-agarose beads were added and incubated for 4 h. After washing, the beads were boiled in SDS buffer, and the released proteins were subjected to SDS–PAGE analysis. A protein band of ~35 kDa was subjected to microcapillary LC/MS/MS for protein identification (Harvard Medical School, Taplin Mass Spectrometry Facility. ProteomeXchange accession: PXD066089). For western blotting and IB, proteins were transferred to nitrocellulose membranes. After blocking with 5% BSA in TBST (pH 7.4), the membranes were incubated with anti-ATP5C antibody (Abcam, MA) at 1:25,000 in 5% BSA/TBST for 16 h at 4 °C. The secondary antibody at 1:1,000 was applied (anti-goat IgG-HRP; Santa Cruz Biotechnology, TX). The signal was detected using enhanced chemiluminescence (ECL, 34580, Invitrogen, MA), and protein bands were visualized by a chemiluminescence imager (ProteinSimple, CA).

Surface plasmon resonance (SPR)

Recombinant human ATP5C with a His-tag at the N-terminus was obtained from Creative Biomart (ATP5F1-37H, NY). It was diluted in running buffer (TBS: 20 mM Tris-HCl, 20 mM NaCl, pH 7.8, 0.005% p20 surfactant) to obtain the ligand samples. Lyophilized aurB peptide was reconstituted with TBS (20 mM Tris-HCl, 80 mM NaCl, pH 7.8); the stock solutions were further diluted in running buffer to obtain the analyte samples. Buffers were prepared using reagents from Sigma–Aldrich Co. with bi-distilled/microfiltered water (Sartorius, Göttingen, Germany). Both samples and buffer solutions were stored at −20 °C and thermalized at room temperature just before experiments.

The SPR experiments were conducted at 25 °C using a Biacore X100 instrument (GE Healthcare, BioSciences AB, Uppsala, Sweden). The sensor chips and chemicals involved in the attachment of the ligand to the chip surface were purchased from Cytiva.

ATP5C was bound on the sensor chip NTA (Nitrilotriacetic acid) by nickel chelation of its poly-histidine tag. The sensor chip surface was prepared with a conditioning cycle using a 1-min pulse of a solution of 350 mM EDTA in running buffer at 10 µl/min. Then, a 0.5 mM solution of $NiCl_2$ was injected at 10 µl/min to form a chelation bond between the nickel ions and NTA immobilized on the surface. With the subsequent 11-min injection of 0.7 µM

ATP5C in 10 mM sodium acetate buffer (pH 4) at a 5 µl/min flow rate, the ligand molecules were captured by their His-tags into the coordination bond with Ni^{2+} and NTA, reaching a binding response of approximately 1000 RU in the measuring flow cell (fc2). The blank immobilization of the reference flow cell (fc1) was conducted by only executing the conditioning cycle. EDTA (3 mM) was employed for the washing steps in the capture procedure, and 50 µM EDTA was included in the running buffer to counteract the effect of contaminant levels of metal ions. Interaction tests were carried out as single-cycle kinetics assays, in which 5 samples with increasing concentrations of aurB (187, 281, 421, 632, 947 µM) were sequentially fluxed at a flow rate of 30 µl/min over the ATP5C-functionalized sensor chip surface for 180 s, separated by 180 s dissociation steps, and followed by a final dissociation of 1200 s. Both capture and analysis procedures were programmed by means of wizard templates and were completely automated. Data evaluation was performed by using BiaEvaluation software 2.1 (GE Healthcare, BIOSciences AB, Uppsala, Sweden). Sensorgrams were double-reference subtracted (Myszka, 1999), *i.e.*, corrected for bulk refractive index changes, drift, jumps due to injection needle positioning and nonspecific interactions by subtracting the response obtained from the reference flow cell, as well as being corrected for systematic noise by subtracting the average blank response obtained from zero concentration cycles, carried out by substituting sample injections with buffer injections. Kinetic parameters were extracted by global fit of the corrected sensorgrams. Fits were evaluated by residual plots, $\chi 2$ values and U values, the latter estimating the uniqueness of the calculated parameters (not significantly correlated for $U < 15$). Measurements were conducted in triplicate.

Confocal microscopy

Similar to the previous report,[93] cells were seeded onto glass slides (Thermo Fisher) placed in 24-well plates at a density of 2×10^4 cells per well and allowed to adhere overnight. The following day, cells were rinsed with PBS and incubated with 20 µM Alexa Fluor 568-conjugated aurB for 2 h at 37 °C. For mitochondrial labeling, cells were subsequently stained with 100 nM MitoTracker Green (M7514, Thermo Fisher, MA) for 20 min. The cells were then fixed in 2% formalin for 10 min. After washing, the slides were mounted using Vectashield mounting medium containing DAPI (94010, Vector Laboratories, CA). Fluorescence images were acquired with a Zeiss LSM 980 confocal laser scanning microscope (Oberkochen, Germany), and image processing was carried out using ZEISS ZEN Lite software version 7.1.

Fluorescence imaging of ATP in prostate cancer cells

DU145, PC3, and CRL-11611 cells were seeded (4×10^5 cells/well) in a confocal chamber and incubated for 24 h. These cell lines were then treated with oligomycin A (5 µM,[94] 11342, Cayman, MI) and aurB (50 µM) for 24 h. One group of cells was cultured in media alone as a control group. Cells were incubated with ATP-Red (10 µM, SCT045, Sigma–Aldrich, MO) at 37 °C for 15 min and then washed three times with PBS before imaging. Fluorescence imaging was performed using a confocal microscope [Zeiss LSM 710 Confocal Microscope (META)].

Complex V activity measurement

Cells were cultured in T-175 flasks. After overnight culture, the cells were washed twice with PBS, and the mitochondrial fraction was prepared with Qproteome Mitochondria Isolation Kits (Qiagen). Protein concentration was measured by the BCA assay kit, and a standard curve was quantified to ensure equal loading and activity measurement (Thermo Fisher). Fifty micrograms of protein from the mitochondrial fraction were used to measure Complex V activity using ATP synthase-specific activity microplate assay kits (ab109717, Abcam, MA) following the manufacturer's instructions.

Seahorse XF analyzer

DU145, PC3, and CRL-11611 cells were plated in Seahorse XF96 Cell Culture Microplates (101085-004, Agilent Technologies, CA) with 1.2×10^4 cells/well for 24 h. Cells were then treated with aurB at different concentrations (50, 75, and 100 µM) for 24 h. Each cell line was incubated at 37 °C in a 5% CO_2 atmosphere for 24 h. Then, 1 h before analysis, the cells were incubated at 37 °C without CO_2 in Seahorse XF DMEM (Agilent Technologies, CA). Mitochondrial respiration (OCR; oxygen consumption rate) and glycolysis (ECAR; extracellular acidification rate) were measured using Seahorse XF Mito Stress Test Kits (103015-100; Agilent Technologies, CA) and Glycolysis Stress Test Kits (103020-100, Agilent Technologies, CA), respectively, on an XFe96 Analyzer (Agilent Technologies, CA) following the manufacturer's instructions.

Xenograft animal models

Human prostate cancer cells (PC3) were injected *s.c.* into the right flanks of 5- to 6-week-old male athymic mice.[95] When tumors reached 5 mm in diameter, animals were randomized into control and treatment groups. The dosages were as follows: paclitaxel (10 mg/kg, once a week),[96] p28 (10 mg/kg daily), and aurB (5 mg/kg daily), *i.p.* All animals were weighed twice a week. At necropsy, tumors were dissected and weighed. Statistical comparisons were performed by one-way analysis of variance (ANOVA) (control vs treatment). Tumor samples were fixed overnight in 10% buffered formalin. Fixation was followed by dehydration, clearing, and infiltration.[19,97] All in vivo studies were reviewed and approved by the University of Illinois at Chicago (UIC) Institutional Animal Care and Use Committee (IACUC) and performed in accordance with the United States Animal Welfare Act and the guidelines of the National Institutes of Health.

Intratibial injection of DU145-luc cells

Intratibial injection was performed as described previously.[98] DU145 cells were cultured in DMEM supplemented with 10% FBS, 100 units/ml penicillin, and 100 µg/ml streptomycin. DU145 cells stably expressing the luciferase gene (pGL4.51[luc2/CMV/Neo], Promega, WI) were generated through chemical transfection using FuGENE HD (Promega) in the presence of G418 antibiotics (GoldBio, MO). The DU145-luc cell line was maintained at 70% confluency and regularly monitored for luminescence activity. DU145-luc cells were resuspended in Matrigel Growth Factor Reduced (Sigma, MA) at a concentration of 5×10^5 cells/20 µl. Intratibial bone injections were performed on 4- to 5-week-old athymic male mice. Briefly, the proximal end of the left tibia was surgically exposed, the knee was flexed, and 20 µl of Matrigel containing DU145-luc cells was injected into the bone marrow space using a 26-gauge needle. After 2 weeks, the mice injected with DU145-luc cells were randomly divided into groups receiving PBS, radiation (focal radiation at 2.0 Gy, X-Rad320), aurB (10 mg/kg, *i.p.*, three times per week), or a combination of radiation (2.0 Gy) and aurB (10 mg/kg, *i.p.*, three times per week) ($N = 5$). Radiation was targeted to the proximal end of the left tibia and administered in a single fraction of 2.0 Gy. The day of radiation was designated day 0 of treatment.

Histological analyses

Samples that were collected were preserved for 24 h using buffered 3.7% formalin (Anatech, NV). After fixation, 70% ethanol was added in place of formalin. Samples were then embedded in paraffin, and blocks were sectioned into 4 µm-thick pieces and placed on slides before being prepared for IHC staining. Ki67 (LabVision, CA) staining was performed on the tissue sections using a Vector Vectastain Elite ABC Kit. The TUNEL assay was performed on the sections using the Millipore Sigma ApopTag Peroxidase In Situ Apoptosis Detection Kit.[19,97] A pathologist who was blinded to experimental groups examined the slides. For quantification of lung metastasis, H&E slides were captured from

the whole tissue section. The images were analyzed by ImageJ software.[99]

In vivo bioluminescence imaging

D-Luciferin potassium salt (LUCK-100, GoldBio, MO) was administered to the mice via intraperitoneal injection at a dose of 150 mg/kg. Following D-luciferin administration, mice were anesthetized with isoflurane in oxygen and placed in position for bioluminescence imaging using a Spectral Lago X system (Accela, Czech Republic). Images were collected for up to 30 min after injection. Regions of interest (ROIs) were defined in Aura software (version 3.2), and total bioluminescent signal within each ROI was quantified. Signal intensity was expressed as radiance (photons/s/cm^2/sr) for each ROI. The radiance values for each animal in the experimental group were plotted to generate tumor growth curves. For X-ray imaging, the anesthetized mice were positioned, and images were captured using the Spectral Lago X imaging system. Aura software was then utilized to merge the X-ray and bioluminescent images.

RNA isolation and expression analysis

RNA from tumor tissues was extracted by RNeasy Mini Kits (Qiagen, MA). Total mRNA expression was measured on an nCounter SPRINT Profiler (NanoString Inc., WA) using the nCounter Human Metabolic Pathways Panel (XT-CSO-HMP1-12, NanoString), covering 768 human mRNAs associated with metabolic processes. For each sample, a hybridization reaction was prepared in a cartridge containing 3 µl of Reporter CodeSet, 5 µl of Hybridization Buffer, 5 µl of RNA sample (50 ng), and 2 µl of Capture ProbeSet at room temperature. The reactions were incubated overnight at 65 °C in a thermocycler to allow hybridization of the RNA targets with the corresponding reporter and capture probes. After hybridization, 35 µl of each reaction mixture was transferred into an nCounter cartridge, which was then sealed and placed in the SPRINT Profiler drawer for processing. Gene expression analysis was carried out using the reporter code count (RCC) files and reporter library files (RLF) generated by the nCounter SPRINT Profiler and analyzed in nSolver Advanced Analysis Software v4.0. Background correction, quality control, and normalization across samples were performed according to the Gene Expression Data Analysis Guidelines (MAN-C0011–04). Imaging quality was considered acceptable when the registered field of view exceeded 75%; lanes below this threshold were flagged. Binding density was flagged when optical features per square micron fell outside the acceptable range of 0.1–1.8. Hybridization performance was assessed using positive control linearity, with samples flagged when the correlation coefficient was less than 0.95. The positive control limit of detection was flagged when counts for the 0.5 fM positive control were no more than two standard deviations above the mean of the negative controls. Background threshold values were defined as the mean count of the manufacturer-provided negative controls plus two standard deviations. Positive control normalization factors were calculated from the geometric mean of the positive controls, and lanes with factors outside the range of 0.3 to 3.0 were flagged. Content normalization was based on the geometric mean of 20 housekeeping genes, with lanes flagged when normalization factors were outside the range of 0.1 to 10.0. Normalized mRNA counts were analyzed for differential expression in four comparative analyses: aurB vs. PBS, combination vs. IR, IR vs. PBS, and combination vs. IR. Differential expression analysis was performed via the nSolver Advanced Analysis module. The raw data were uploaded to the Gene Expression Omnibus platform (Accession: GSE285854).

Statistical analysis

To ensure robust and unbiased results, the study incorporated appropriate statistical analyses, prospectively determined sample sizes and replication numbers, suitable positive and negative controls, and blinded experimental procedures. Data are presented as the mean ± SEM. The animal models proposed in this application included randomization and multiple experimental models to maintain scientific integrity and reproducibility. Data processing and statistical analysis were conducted using GraphPad Prism version 10 (GraphPad Software, MA). Two-sided testing was performed for each analysis, and $p < 0.05$ was considered statistically significant. n.s., not significant, * $p < 0.05$, ** $p < 0.01$, *** $p < 0.001$.

DATA AVAILABILITY

The gene expression profiles described in this study can be found at the Gene Expression Omnibus, which is available online. Accession number: GSE285854. The proteomics data were deposited to the ProteomeXchange Consortium via the PRIDE partner repository under the following dataset identifier: PXD066089.

ACKNOWLEDGEMENTS

This work made use of facilities in the Biological Resources Laboratory, Preclinical Imaging Core, Cardiovascular Research Core, and Flow Cytometry Core (Research Resources Center, UIC). We thank Drs. R. R. Mehta and C. W. Beattie for their suggestions at the early phase of the project. Parts of this work were presented at the 2017 AACR Annual Meeting in Washington, DC. Figures 1, 6a, 7a, Figure cd, and Supplementary Fig. S1b were generated by BioRender (BioRender.com, ON, Canada). This research was partly supported by the NIH/National Cancer Institute (R01CA272564, R01CA289701, and R21CA280814) to TY. Dr. Tapas K. Das Gupta participated in intellectually developing this article before he passed away on December 17, 2024.

AUTHOR CONTRIBUTIONS

Conceptualization and Study Design: S.A.N., D.B.T., S.C., A.R.B., T.K.D.G., T.Y. Data collection and Analysis: S.A.N., D.B.T., D.J.R., V.B., K.C., A.G., W.L., N.H.T.P., T.Y. Writing draft and Editing: S.A.N., D.B.T., S.C., A.R.B., T.Y. All authors have read and approved the article.

ADDITIONAL INFORMATION

Supplementary information The online version contains supplementary material available at https://doi.org/10.1038/s41392-026-02703-7.

Competing interests: The authors declare no competing interests.

Publisher's note Springer Nature remains neutral with regard to jurisdictional claims in published maps and institutional affiliations.

REFERENCES

1. Zong, W.-X., Rabinowitz, J. D. & White, E. Mitochondria and cancer. *Mol. cell* **61**, 667–676 (2016).
2. Wang, F., Ogasawara, M. A. & Huang, P. Small mitochondria-targeting molecules as anticancer agents. *Mol. Asp. Med.* **31**, 75–92 (2010).
3. Speransky, S. et al. A novel RNA aptamer identifies plasma membrane ATP synthase beta subunit as an early marker and therapeutic target in aggressive cancer. *Breast Cancer Res. Treat.* **176**, 271–289 (2019).
4. Sotgia, F. & Lisanti, M. P. Mitochondrial mRNA transcripts predict overall survival, tumor recurrence and progression in serous ovarian cancer: Companion diagnostics for cancer therapy. *Oncotarget* **8**, 66925–66939 (2017).
5. Aubrey, B. J., Kelly, G. L., Janic, A., Herold, M. J. & Strasser, A. How does p53 induce apoptosis and how does this relate to p53-mediated tumor suppression? *Cell Death Differ.* **25**, 104–113 (2018).
6. Cha, H.-R., Lee, J. H. & Ponnazhagan, S. Revisiting immunotherapy: A focus on prostate cancer. *Cancer Res.* **80**, 1615–1623 (2020).
7. McCutcheon, J. P. From microbiology to cell biology: when an intracellular bacterium becomes part of its host cell. *Curr. Opin. cell Biol.* **41**, 132–136 (2016).
8. Gray, M. W. Lynn Margulis and the endosymbiont hypothesis: 50 years later. *Mol. Biol. Cell* **28**, 1285–1287 (2017).
9. Zoschke, R. & Bock, R. Chloroplast translation: Structural and functional organization, operational control, and regulation. *Plant cell* **30**, 745–770 (2018).
10. Boguszewska, K., Szewczuk, M., Kazmierczak-Baranska, J. & Karwowski, B. T. The similarities between human mitochondria and bacteria in the context of structure, genome, and base excision repair system. *Molecules* **25**, 2857 (2020).

11. Carrie, C. & Small, I. A reevaluation of dual-targeting of proteins to mitochondria and chloroplasts. *Biochim. et. Biophys. Acta (BBA) - Mol. Cell Res.* **1833**, 253–259 (2013).
12. Murphy, M. E., Lindley, P. F. & Adman, E. T. Structural comparison of cupredoxin domains: domain recycling to construct proteins with novel functions. *Protein Sci.* **6**, 761–770 (1997).
13. Stevens, F. J. Homology versus analogy: possible evolutionary relationship of immunoglobulins, cupredoxins, and Cu,Zn-superoxide dismutase. *J. Mol. Recognit.: JMR* **21**, 20–29 (2008).
14. Savelieff, M. G. et al. Experimental evidence for a link among cupredoxins: Red, blue, and purple copper transformations in nitrous oxide reductase. *Proc. Natl. Acad. Sci.* **105**, 7919–7924 (2008).
15. Makarenko, M. et al. The investigation of perennial sunflower species (*Helianthus* L.) mitochondrial genomes. *Genes (Basel)* **11**, 982 (2020).
16. Haehnel, W., Ratajczak, R. & Robenek, H. Lateral distribution and diffusion of plastocyanin in chloroplast thylakoids. *J. Cell Biol.* **108**, 1397–1405 (1989).
17. De Rienzo, F., Gabdoulline, R. R., Menziani, M. C. & Wade, R. C. Blue copper proteins: a comparative analysis of their molecular interaction properties. *Protein Sci.: a Publ. Protein Soc.* **9**, 1439–1454 (2000).
18. Murphy, L. M., Dodd, F. E., Yousafzai, F. K., Eady, R. R. & Hasnain, S. S. Electron donation between copper containing nitrite reductases and cupredoxins: the nature of protein–protein interaction in complex formation. *J. Mol. Biol.* **315**, 859–871 (2002).
19. Yamada, T. et al. Bacterial redox protein azurin, tumor suppressor protein p53, and regression of cancer. *Proc. Natl. Acad. Sci. USA* **99**, 14098–14103 (2002).
20. Yamada, T. et al. The bacterial redox protein azurin induces apoptosis in J774 macrophages through complex formation and stabilization of the tumor suppressor protein p53. *Infect. Immun.* **70**, 7054–7062 (2002).
21. Pseudomonas gives cancer cells the blues. *Science's STKE* **2002**, tw416-tw416 (2002).
22. Jia, L. et al. Preclinical pharmacokinetics, metabolism, and toxicity of azurin-p28 (NSC745104) a peptide inhibitor of p53 ubiquitination. *Cancer Chemother. Pharmacol.* **68**, 513–524 (2011).
23. Yamada, T., Das Gupta, T. K. & Beattie, C. W. p28, an anionic cell-penetrating peptide, increases the activity of wild type and mutated p53 without altering its conformation. *Mol. Pharm.* **10**, 3375–3383 (2013).
24. Yamada, T. et al. A peptide fragment of azurin induces a p53-mediated cell cycle arrest in human breast cancer cells. *Mol. Cancer Ther.* **8**, 2947–2958 (2009).
25. Yamada, T., Signorelli, S., Cannistraro, S., Beattie, C. W. & Bizzarri, A. R. Chirality switching within an anionic cell-penetrating peptide inhibits translocation without affecting preferential entry. *Mol. Pharm.* **12**, 140–149 (2015).
26. Yamada, T., Das Gupta, T. K. & Beattie, C. W. p28-mediated activation of p53 in G2–M phase of the cell cycle enhances the efficacy of DNA damaging and antimitotic chemotherapy. *Cancer Res.* **76**, 2354–2365 (2016).
27. Warso, M. A. et al. A first-in-class, first-in-human, phase I trial of p28, a non-HDM2-mediated peptide inhibitor of p53 ubiquitination in patients with advanced solid tumors. *Br. J. Cancer* **108**, 1061–1070 (2013).
28. Lulla, R. et al. Phase 1 trial of p28 (NSC745104), a non-HDM2 mediated peptide inhibitor of p53 ubiquitination in children with recurrent or progressive CNS tumors: A final report from the pediatric brain tumor consortium. *Neuro Oncol.* **18**(9), 1319–1325 (2016).
29. Razzak, M. One step closer to drugging p53. *Nat. Rev. Clin. Oncol.* **10**, 246 (2013).
30. Blankenship, R. E. Early evolution of photosynthesis. *Plant Physiol.* **154**, 434–438 (2010).
31. Mitchell, S. L., Blumberg, E. A. & Edelstein, P. H. Bacteremia caused by the photosynthetic environmental bacterium Rhodopseudomonas. *J. Infect. Chemother.* **23**, 720–723 (2017).
32. Di Rienzi, S. C. et al. The human gut and groundwater harbor nonphotosynthetic bacteria belonging to a new candidate phylum sibling to Cyanobacteria. *Elife* **2**, e01102 (2013).
33. McManus, J. D. et al. Isolation, characterization, and amino acid sequences of auracyanins, blue copper proteins from the green photosynthetic bacterium *Chloroflexus aurantiacus*. *J. Biol. Chem.* **267**, 6531–6540 (1992).
34. Van Driessche, G. et al. Auracyanin A from the thermophilic green gliding photosynthetic bacterium *Chloroflexus aurantiacus* represents an unusual class of small blue copper proteins. *Protein Sci.: a Publ. Protein Soc.* **8**, 947–957 (1999).
35. Sepich-Poore, G. D. et al. The microbiome and human cancer. *Science* **371**, eabc4552 (2021).
36. Cullin, N., Azevedo Antunes, C., Straussman, R., Stein-Thoeringer, C. K. & Elinav, E. Microbiome and cancer. *Cancer Cell* **39**, 1317–1341 (2021).
37. Choi, J. K. et al. Cross-talk between cancer and *Pseudomonas aeruginosa* mediates tumor suppression. *Commun. Biol.* **6**, 16 (2023).
38. Nejman, D. et al. The human tumor microbiome is composed of tumor type-specific intracellular bacteria. *Science* **368**, 973–980 (2020).
39. Yeo, K. et al. A comparison between full-length 16S rRNA Oxford nanopore sequencing and Illumina V3-V4 16S rRNA sequencing in head and neck cancer tissues. *Arch. Microbiol* **206**, 248 (2024).
40. German, R. et al. Exploring breast tissue microbial composition and the association with breast cancer risk factors. *Breast Cancer Res.* **25**, 82 (2023).
41. Yamada, T. et al. Internalization of bacterial redox protein azurin in mammalian cells: Entry domain and specificity. *Cell. Microbiol.* **7**, 1418–1431 (2005).
42. Taylor, B. N. et al. Noncationic peptides obtained from azurin preferentially enter cancer cells. *Cancer Res.* **69**, 537–546 (2009).
43. Naffouje, S. A., Yamada, T. & Gupta, T. K. D. A peptide derived from a photosynthetic cupredoxin protein, auracyanin, induces a p53-independent apoptosis in cancer cells. *Cancer Res.* **77**, 2311–2311 (2017).
44. Mitsiades, N. A road map to comprehensive androgen receptor axis targeting for castration-resistant prostate cancer. *Cancer Res.* **73**, 4599–4605 (2013).
45. Kirby, M., Hirst, C. & Crawford, E. D. Characterizing the castration-resistant prostate cancer population: A systematic review. *Int. J. Clin. Pract.* **65**, 1180–1192 (2011).
46. Terrisse, S. et al. Overall survival in men with bone metastases from castration-resistant prostate cancer treated with bone-targeting radioisotopes: A meta-analysis of individual patient data from randomized clinical trials. *JAMA Oncol.* **6**, 206–216 (2020).
47. Kratzer, T. B. et al. Prostate cancer statistics, 2025. *CA: A Cancer J. Clin.* **75**, 485–497 (2025).
48. Robert, C. A decade of immune-checkpoint inhibitors in cancer therapy. *Nat. Commun.* **11**, 3801–3801 (2020).
49. Zhang, Z., Li, M., Wang, H., Agrawal, S. & Zhang, R. Antisense therapy targeting MDM2 oncogene in prostate cancer: Effects on proliferation, apoptosis, multiple gene expression, and chemotherapy. *Proc. Natl. Acad. Sci. USA* **100**, 11636–11641 (2003).
50. Shiri, R., Yari, F., Ahmadinejad, M., Vaeli, S. & Tabatabaei, M. R. The caspase-3 inhibitor (peptide Z-DEVD-FMK) affects the survival and function of platelets in platelet concentrate during storage. *Blood Res.* **49**, 49–53 (2014).
51. El Gaafary, M. et al. Prenylated xanthones from mangosteen (*Garcinia mangostana*) target oxidative mitochondrial respiration in cancer cells. *Biomed. Pharmacother.* **179**, 117365 (2024).
52. Levine, A. J., Momand, J. & Finlay, C. A. The p53 tumor suppressor gene. *Nature* **351**, 453–456 (1991).
53. Chendil, D., Srinivasan, S. & Ranga, R. Apoptosis regulation by androgen receptor (AR) in prostate cancer biology. *Cancer Res.* **66**, 349–349 (2006).
54. Wang, X., Deng, H., Basu, I. & Zhu, L. Induction of androgen receptor-dependent apoptosis in prostate cancer cells by the retinoblastoma protein. *Cancer Res.* **64**, 1377–1385 (2004).
55. Tran, D. B. et al. Intracellular redistribution of cell-penetrating peptide p28: A mechanism for enhanced anticancer activity. *J. Controlled Release* **382**, 113660 (2025).
56. Huang, K. et al. Size-dependent localization and penetration of ultrasmall gold nanoparticles in cancer cells, multicellular spheroids, and tumors in vivo. *ACS Nano* **6**, 4483–4493 (2012).
57. Friedman, J. R. & Nunnari, J. Mitochondrial form and function. *Nature* **505**, 335–343 (2014).
58. Wang, J. et al. Involvement of the mitochondrial pathway in p53-independent apoptosis induced by p28GANK knockdown in Hep3B cells. *Cytogenetic genome Res.* **125**, 87–97 (2009).
59. Vaseva, A. V. & Moll, U. M. The mitochondrial p53 pathway. *Biochim. et. Biophys. Acta* **1787**, 414–420 (2009).
60. Herst, P. M., Tan, A. S., Scarlett, D.-J. G. & Berridge, M. V. Cell surface oxygen consumption by mitochondrial gene knockout cells. *Biochim. et. Biophys. Acta (BBA) - Bioenerg.* **1656**, 79–87 (2004).
61. Gartrell, B. A. et al. Metastatic prostate cancer and the bone: Significance and therapeutic options. *Eur. Urol.* **68**, 850–858 (2015).
62. Lane, D. P. Cancer. p53, guardian of the genome. *Nature* **358**, 15–16 (1992).
63. Liu, A. Y. Differential expression of cell surface molecules in prostate cancer cells. *Cancer Res.* **60**, 3429–3434 (2000).
64. Wilson, W. R. & Hay, M. P. Targeting hypoxia in cancer therapy. *Nat. Rev. Cancer* **11**, 393–410 (2011).
65. Mudassar, F., Shen, H., O'Neill, G. & Hau, E. Targeting tumor hypoxia and mitochondrial metabolism with anti-parasitic drugs to improve radiation response in high-grade gliomas. *J. Exp. Clin. Cancer Res.* **39**, 208 (2020).
66. Huang, R. & Zhou, P.-K. HIF-1 signaling: A key orchestrator of cancer radioresistance. *Radiat. Med. Prot.* **1**, 7–14 (2020).
67. Zhao, F., Ming, J., Zhou, Y. & Fan, L. Inhibition of Glut1 by WZB117 sensitizes radioresistant breast cancer cells to irradiation. *Cancer Chemother. Pharmacol.* **77**, 963–972 (2016).

68. Toufektchan, E. & Toledo, F. The guardian of the genome revisited: p53 downregulates genes required for telomere maintenance, DNA repair, and centromere structure. *Cancers (Basel)* **10**, 135 (2018).
69. Muller, P. A. J. & Vousden, K. H. Mutant p53 in cancer: new functions and therapeutic opportunities. *Cancer cell* **25**, 304–317 (2014).
70. Issaeva, N. et al. Rescue of mutants of the tumor suppressor p53 in cancer cells by a designed peptide. *Proc. Natl. Acad. Sci.* **100**, 13303–13307 (2003).
71. Tai, S. et al. PC3 is a cell line characteristic of prostatic small cell carcinoma. *Prostate* **71**, 1668–1679 (2011).
72. Hu, J., Han, B. & Huang, J. Morphologic spectrum of neuroendocrine tumors of the prostate: An updated review. *Arch. Pathol. Lab. Med.* **144**, 320–325 (2019).
73. Ferguson, A. et al. Immunogenomic landscape of neuroendocrine prostate cancer (NEPC). *J. Clin. Oncol.* **37**, 224–224 (2019).
74. Cancer Facts & Figures 2020. *American Cancer Society* 1–70 (2020).
75. Gupta, N., Gupta, P. & Srivastava, S. K. Penfluridol overcomes paclitaxel resistance in metastatic breast cancer. *Sci. Rep.* **9**, 5066 (2019).
76. Williams, C. & Bryant, A. Short versus long duration infusions of paclitaxel for any advanced adenocarcinoma. *Cochrane Database Syst. Rev.* CD003911-CD003911 (2011).
77. Richard, J. P. et al. Cell-penetrating peptides. A reevaluation of the mechanism of cellular uptake. *J. Biol. Chem.* **278**, 585–590 (2003).
78. Hao, M., Zhang, L. & Chen, P. Membrane internalization mechanisms and design strategies of Arginine-rich Cell-Penetrating Peptides. *Int. J. Mol. Sci* **23**, 9038 (2022).
79. Madani, F. & Gräslund, A. Membrane molecular interactions and induced structures of CPPs. *Methods Mol. Biol. (Clifton, N. J.)* **2383**, 153–165 (2022).
80. Yang, D., Liu, B. & Sha, H. Advances and prospects of cell-penetrating peptides in tumor immunotherapy. *Sci. Rep.* **15**, 3392 (2025).
81. Giddings, E. L. et al. Mitochondrial ATP fuels ABC transporter-mediated drug efflux in cancer chemoresistance. *Nat. Commun.* **12**, 2804 (2021).
82. Fiorillo, M., Ózsvári, B., Sotgia, F. & Lisanti, M. High ATP production fuels cancer drug resistance and metastasis: Implications for mitochondrial ATP depletion therapy. *Front. Oncol.* **11**, 740720 (2021).
83. Fiorillo, M., Scatena, C., Naccarato, A. G., Sotgia, F. & Lisanti, M. P. Bedaquiline, an FDA-approved drug, inhibits mitochondrial ATP production and metastasis in vivo, by targeting the gamma subunit (ATP5F1C) of the ATP synthase. *Cell Death Differ.* **28**, 2797–2817 (2021).
84. Gogvadze, V., Orrenius, S. & Zhivotovsky, B. Mitochondria in cancer cells: what is so special about them? *Trends cell Biol.* **18**, 165–173 (2008).
85. Modica-Napolitano, J. S. & Singh, K. K. Mitochondrial dysfunction in cancer. *Mitochondrion* **4**, 755–762 (2004).
86. Fulda, S., Galluzzi, L. & Kroemer, G. Targeting mitochondria for cancer therapy. *Nat. Rev. Drug Discov.* **9**, 447–464 (2010).
87. Feichtinger, R. G. et al. Reduced levels of ATP synthase subunit ATP5F1A correlate with earlier-onset prostate cancer. *Oxid. Med. Cell. Longev.* **2018**, 1347174 (2018).
88. Sotgia, F. & Lisanti, M. P. Mitochondrial markers predict survival and progression in non-small cell lung cancer (NSCLC) patients: Use as companion diagnostics. *Oncotarget* **8**, 68095–68107 (2017).
89. Li, W. et al. Ectopic expression of the ATP synthase β subunit on the membrane of PC-3 M cells supports its potential role in prostate cancer metastasis. *Int. J. Oncol.* **50**, 1312–1320 (2017).
90. Wang, T., Ma, F. & Qian, H. L. Defueling the cancer: ATP synthase as an emerging target in cancer therapy. *Mol. Ther. Oncolytics* **23**, 82–95 (2021).
91. Mehta, R. R. et al. In vitro transformation of human congenital naevus to malignant melanoma. *Melanoma Res.* **12**, 27–33 (2002).
92. Rauth, S., Kichina, J., Green, A., Bratescu, L. & Das Gupta, T. K. Establishment of a human melanoma cell line lacking p53 expression and spontaneously metastasizing in nude mice. *Anticancer Res* **14**, 2457–2463 (1994).
93. Mander, S. et al. Improvement of DCIS resection using intraoperative imaging with ICG-p28. *Sci. Rep.* **16**, 3136 (2025).
94. Tourmente, M., Sansegundo, E., Rial, E. & Roldan, E. R. S. Capacitation promotes a shift in energy metabolism in murine sperm. *Front. Cell Dev. Biol.* **10**, 950979 (2022).
95. Yamada, T. et al. p28, a first in class peptide inhibitor of cop1 binding to p53. *Br. J. Cancer* **108**, 2495–2504 (2013).
96. El Hilali, N., Rubio, N. & Blanco, J. Different effect of paclitaxel on primary tumor mass, tumor cell contents, and metastases for four experimental human prostate tumors expressing luciferase. *Clin. Cancer Res.* **11**, 1253–1258 (2005).
97. Punj, V. et al. Bacterial cupredoxin azurin as an inducer of apoptosis and regression in human breast cancer. *Oncogene* **23**, 2367–2378 (2004).
98. Zhang, B., Li, X., Qian, W. P., Wu, D. & Dong, J. T. Measurement of bone metastatic tumor growth by a tibial tumorigenesis assay. *Bio Protoc.* **11**, e4231 (2021).
99. Chang, J. & Erler, J. T. in *Tumor Microenvironment*. (eds C. Koumenis, L. M. Coussens, A. Giaccia, & E. Hammond) 245-251 (Springer International Publishing).
100. Zimmerman, J. M., Eliezer, N. & Simha, R. The characterization of amino acid sequences in proteins by statistical methods. *J. Theor. Biol.* **21**, 170–201 (1968).